Laminin-defined Mechanical Status Modulates Retinal Pigment Epithelium Functionality

Aleksandra N. Kozyrina*[1, 2], Teodora Piskova*[1, 2], Francesca Semeraro[1, 2], Iris Doolaar[3], Taspia Prapty[1, 2], Tamás Haraszti[3], Maxime Hubert[4, 5], Reinhard Windoffer[2], Rudolf Leube[2], Ana-Sunčana Smith[4, 5] and Jacopo Di Russo[1, 2, 3]

* equal contribution

1. Interdisciplinary Centre for Clinical Research, RWTH Aachen University, Pauwelstrasse 30, 52074 Aachen, Germany.
2. Institute of Molecular and Cellular Anatomy, RWTH Aachen University, Wendlingweg 2, 52074 Aachen, Germany.
3. DWI – Leibniz-Institute for Interactive Materials, Forckenbeckstrasse 50, 52074 Aachen, Germany.
4. PULS Group, Department of Physics and Interdisciplinary Center for Nanostructured Films, Friedrich-Alexander University of Erlangen-Nürnberg, 91058 Erlangen, Germany.
5. Group for Computational Life Sciences, Division of Physical Chemistry, Rudjer Bošković Institute,10000 Zagreb, Croatia.

Correspondence:

Jacopo Di Russo

jdirusso@ukaachen.de

ABSTRACT

Epithelial cells are highly interconnected, whereby they acquire mesoscale mechanical properties to accomplish specific tissue functions. In homeostasis, this mechanical status can be summarised as mechanical homeostasis, regulated by the balance of intercellular tension and extracellular matrix adhesion forces. In the outer retina, the significance of these forces in defining its mechanical homeostasis and consequences for vision remains poorly understood. The retinal pigmented epithelium (RPE) is located at the base of the retina and supports vision by ensuring the light sensitivity and lifespan of photoreceptor cells. Given the varying photoreceptor densities along the visual angle, this functional demand on the RPE varies from the most illuminated macula to the less illuminated retinal periphery and corresponds to a significant difference in monolayer organisation. In this work, we hypothesised that extracellular matrix cues define the relation between RPE organisation, mechanical status and functional capacity. We found that the density of basement membrane laminins modulates the level of RPE contractility, which directly controls the efficiency of the epithelium in phagocytosing photoreceptor outer segments. *In vivo*, the density gradient of laminin α5 and 332 follow retinal functional demand, thus supporting the physiological role of laminins in controlling RPE mechanical homeostasis. Our data suggest that laminin density and isoforms can differentially engage integrins β1 and β4, the ratio of which, in turn, determines the contribution of actin vs keratin cytoskeleton in balancing tissue mechanics. ECM-defined mechanical status of the RPE provides a novel parameter for visual function. It opens new paths of investigation and treatment for sight-threatening diseases such as high myopia and age-related macular degeneration.

The mechanical properties of any tissue define its function and state [1,2]. In a homeostatic state, these mechanical features are maintained in a preferred range for optimal activity, also known as tissue mechanical homeostasis [3]. One of the main players in defining the mechanical homeostasis of tissues is its extracellular matrix (ECM) composition [4,5]. The most prominent ECM layer in the retina is the Bruch's membrane that connects the choroidal vessels to the neural retina and the pigment epithelium (RPE), altogether called as outer retina [6].

The RPE is a postmitotic cell monolayer is in direct contact with the light-detecting neural tissue. In the developing eye, the RPE organises the retina [7,8], while in the adult, it plays a key role in the visual cycle [9,10]. One of the main activities of each RPE cell is the daily phagocytosis of shed photoreceptors fragments, therefore mediating the constant renewal of light-sensitive outer segments and ensuring photoreceptor lifespan and light sensitivity [11–13]. The number of POS per RPE cells is not constant within the eye, with an average of 25-30 POS per RPE cell in the central and macular area and decreasing towards the periphery (~ 15 POS) [14], indicating a gradient of functional demand. RPE cells are polygonal in shape and tightly adhere to each other; they arrange as a honeycomb-like structure in the centre, which gradually shifts to a more elongated and less organised structure towards the retinal periphery, suggesting a change in its mechanical status [15–17]. The RPE is tightly bound to its underlying basement membrane, part of the more complex Bruch's membrane. The thickness of the Bruch's membrane and its content of fibrillar collagens and elastin are known to vary from the centre to the periphery [18,19]. Nevertheless, to date, it is still unclear how this affects overall mechanical properties of the ECM and, more importantly, whether this regional variability is also present for RPE basement membrane components. Furthermore, whether any relation exists between ECM heterogeneity and RPE mechanical homeostasis is still an open question.

Here, we hypothesise that the spatial variation of Bruch's membrane cues controls the RPE mechanical status and the region-dependent functional capacity. Our characterisation of the Bruch's membrane composition in mice reveals a relative spatial density reduction of specific basement membrane laminins towards the retinal periphery. The decreased density of laminin 511 and not laminin 332 reduces POS phagocytic efficiency in stem cell-derived RPE monolayers obtained on soft polyacrylamide hydrogels. This is associated with increased RPE contractility, quantified by traction force and monolayer stress microscopy. By varying the hydrogel's stiffness, coating, and cellular actomyosin activity, we show that POS phagocytosis efficiency depends on the level of RPE contractility. Finally, adhesion assay and flow cytometry data demonstrate that the higher contractility status corresponds to a lower integrin β4/β1 ratio at low laminin 511 density. Changes in keratin network organization *in vivo* support the presence of different epithelial mechanical status and suggest

spatial variations of integrin β4/β1 ratio, emphasising a pivotal role of keratin vs actin cytoskeleton balance to maintain RPE mechanical homeostasis.

These findings underline for the first time the importance of mechanical homeostasis in RPE and, in general, in the outer retina. The significance of RPE mechanical status for visual function in adults opens the question of its role in ageing and sight-threatening diseases such as (high) myopia and age-related macular degeneration. Finally, this study could incentivize a larger use of Rho kinase inhibitors, currently used as anti-glaucoma medications, for other retinal diseases.

RESULTS

The Bruch's membrane presents biochemical heterogeneity correlating with different mechanical status of the RPE.

To understand the possible relation of ECM biochemical and mechanical cues with RPE mechanobiology, we characterised the Bruch's membrane of adult BALB/C mice (25-30 weeks) (Fig 1). Bruch's membrane, retinal complexity and function have been described in relation to the sightline or visual axis [14,17]. In both mice and humans, the central region (macula in humans) exhibits the highest density of photoreceptor cells and the highest photoreceptor to RPE ratio. This ratio gradually decreases with the radial distance from the optic nerve, signifying a reduction in RPE functional demand [14]. Hence, we identified three regions with respect to the radial distance from the optic nerve: centre (300-1200 μm), mid periphery (1200-2000 μm) and far periphery (2000-3000 μm) (Fig. 1 A). We observed substantial alteration in the organisation of RPE cell along the radial distance (Fig. 1 A), which is consistent with previous reports [15–17]. From a classic honeycomb arrangement in the centre, the RPE gradually changes to a monolayer consisting of more elongated cells at the far periphery (Fig. 1 A; Sup fig. 1 A, D) [15–17].

The topology and morphology of an epithelial monolayer define its mechanical properties [20–22]. Hence, we performed morphometric characterisation of the RPE cells in the different regions of the retina (Fig.1 B - D, sup. fig. 1 A - H). RPE cells have the largest area and perimeter in the central region (A = 469 μm^2; P = 84 μm), whereas they become smaller in the mid periphery (A = 349 μm^2; P = 74 μm) and far periphery (A = 343 μm^2; P = 75 μm) (Sup. fig.1 F, G). Next, to better quantify the mechanical consequences of the differential cell arrangement, we calculated the shape factor for each cell, defined as the cell perimeter P divided by the square root of the corresponding cell area A. This density-independent shape factor has been theorised to describe epithelial rigidity based on the balance between cortical tension and cell-cell adhesion energy, with lower values where the first element is more prominent [23]. Our data show an average value in the retinal central region of 3.8, which gradually increases till reaching values over 4.0 at the far periphery. This implies a gradual increase of intercellular

tension, coinciding with the decreasing RPE functional demand (Fig. 1 B, C, sup. fig. 1 E) [14]. Additionally, the comparison of nuclear geometry in the central and far peripheral regions supports the existence of different levels of intracellular strain (sup. fig. 1 I-K). Finally, we noticed the presence of two distinct cell populations in the centre and mid-periphery, which are visible when cell area and cell perimeter distributions are normalised and compared (Fig. 1 D, sup. fig. 1 H). Hence, we compared the RPE topological relations across retinal regions by plotting the rescaled cell areas and perimeters as a function of their number of neighbours (respectively Lewis' law [24–27] and Desh's law [28]) (Fig. 1 E, sup. fig. 1 M). Both comparisons show different curve behaviour in the retinal regions, especially evident between the centre and far periphery.

We then correlated the number of neighbours *(n)* of each cell and the average number of neighbours *m(n)* of any adjacent cells to the first with *n* sides (Aboav-Weaire's laws) (Fig. 1 F) [29–31]. This relation describes the topology of epithelial monolayers via the topological parameter *b(n)* (see method section). The different regions show a linear relationship, as in any functional epithelium [22,29–31]. Nevertheless, a shift is visible between values, suggesting a topological variation of RPE from the centre to the far periphery (Fig. 1 F, sup. fig. L). Altogether, the extensive image-based morphometric and topological analyses (of more than 5500 cells from three mice) strongly support the existence of different mechanical status in the monolayer from the retinal central region to the far periphery.

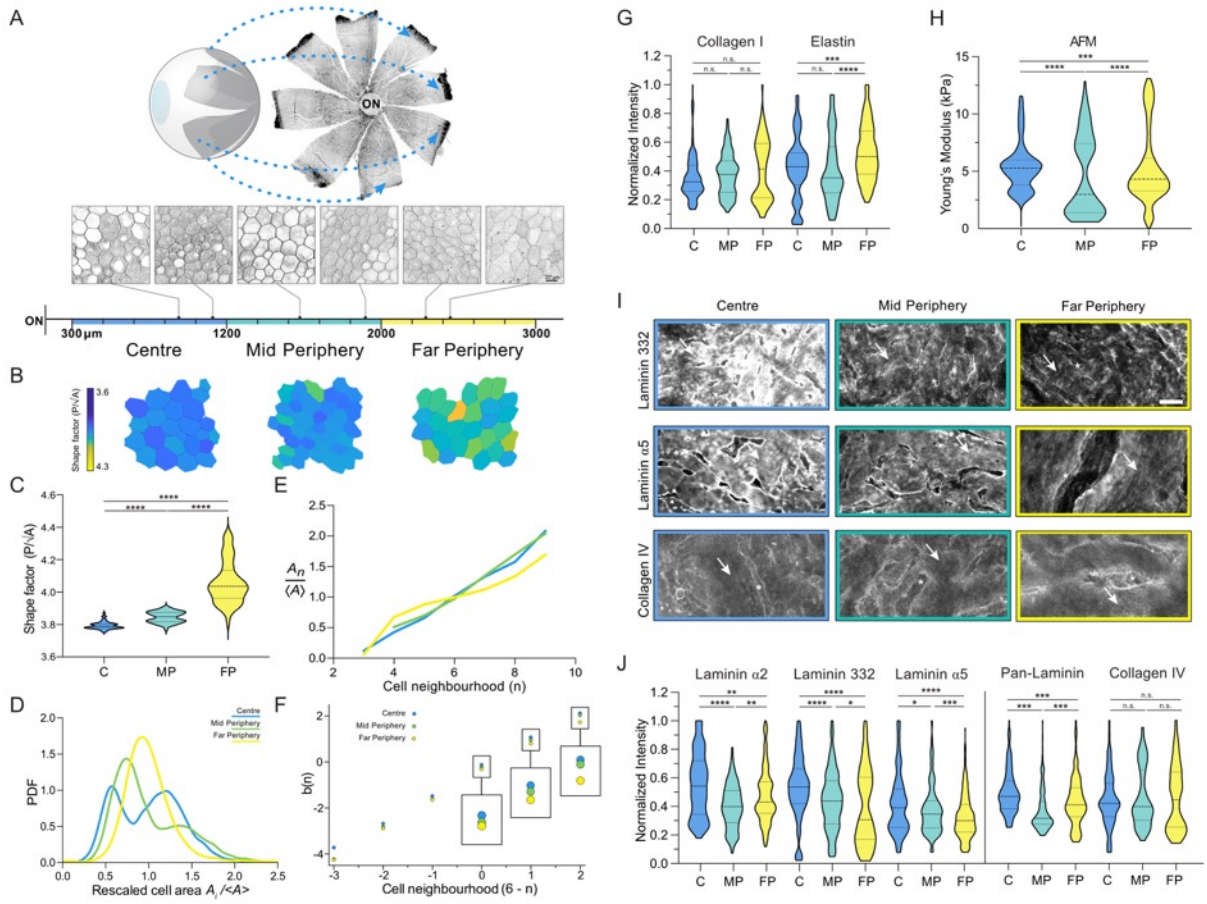

Figure 1: Spatial heterogeneity of murine retinal pigment epithelium topology and Bruch's membrane composition. ***(A)*** *Murine retina flat mount indicating the regions used for analyses and representative F-actin staining of RPE. The regions were defined by the distance from the optic nerve head: centre (300 – 1200 µm), mid periphery (1200 – 2000 µm) and far periphery (2000 – 3000 µm).* ***(B)*** *Representative cell shape index maps for the three regions. The shape index is identified as the perimeter divided by the square root of the area for each cell.* ***(C)*** *Violin plot of mean RPE shape factors from the different regions of the eye analysed from 7 mice.* ***(D)*** *The probability density function (PDF) of the rescaled cell areas defined by $A_i/\langle A\rangle$, A_i being the individual cell area and $\langle A\rangle$ being the average cell area within a given image. More than 5500 cells were analysed from 3 mice.* ***(E)*** *Lewis' law representing the relationship between rescaled cell area and neighbourhood varying for three different regions from 3 mice.* ***(F)*** *Aboav-Weaire's laws showing the variation of the topological parameter b(n) depending on the number of neighbours for each cell between different retinal regions from 3 mice.* ***(G)*** *Violin plots of mean fluorescence intensity of interstitial matrix components of the Bruch's membrane. Data were collected from 3 mice and normalized to the highest intensity per mouse.* ***(H)*** *Violin plots of the regional Young's modulus of the Bruch's membrane from 5 mice.* ***(I)*** *Representative immunofluorescent images of the Bruch's membrane stained for laminin-332, laminin $\alpha5$ and collagen type IV. Arrows and stars indicate RPE basement membrane surface and preparation artefacts respectively. Scale bar 20 µm.* ***(J)*** *Violin plots of mean fluorescence intensity of basement membrane components: laminin $\alpha2$, laminin 332, laminin $\alpha5$, pan-laminin, and collagen type IV. Each region contains the quantification of at least 7 sectors from a minimum of 3 to 6 mice. The data were statistically tested with Mann-Whitney test: *p < 0.05; ** p < 0.01; *** p < 0.001; **** p < 0.0001; n.s. = not significant.*

Next, we were curious to know whether the quantified mechanical gradient of RPE finds a correlation with the distribution of mechanical and biochemical cues within Bruch's membrane. In the epithelial ECM, mechanical cues are mostly determined by the composition and crosslinking density of the interstitial matrix [5]. Therefore, we use confocal microscopy and immunofluorescence staining to quantify the amount of collagen type I and elastin present in the Bruch's membrane. The average intensity quantification of the retina's central, mid peripheral, and far peripheral regions are comparable with the data reported in the literature [18,19] (Fig. 1 G). Next, we quantified the Young's modulus of the Bruch's membrane in different regions using atomic force microscopy (AFM) and indenting into the decellularised ECM by 200 nm. The quantification resulted in a highly variable distribution of the data, with the centre having the most frequent (mode) stiffness of 5.5 kPa, the mid periphery 1.5 kPa and the far periphery 4 kPa (Fig. 1 H). This biphasic stiffness trend suggests that ECM mechanical cues may not be the primary factor governing RPE mechanical homeostasis concerning functional demand.

From the biochemical point of view, the basement membrane provides cues to epithelia regulating its homeostasis with a key role of the different laminin isoforms [5]. Thus, we characterised the composition and relative amount of the main basement membrane components in the Bruch's membrane, namely laminins and collagen type IV (Fig. 1 I, J). Notably, we detected a significant change in the amount of laminin isoforms along the visual axis, whereas collagen type IV remained unchanged. This supports the idea of the importance of laminins in the differential biochemical signalling to the RPE. Among the laminin isoforms detected in Bruch's membrane, we noticed a biphasic trend for laminin $\alpha2$-containing isoforms, with higher (fluorescence) intensity in the centre and far periphery and lower in the mid periphery. On the contrary, isoforms containing laminin 332 and laminin $\alpha5$ were found to have the

109 highest (fluorescence) intensity in the centre and gradually decrease towards the periphery (Fig. 1 I, J).
110 No laminin α1- or α4-containing isoforms were detected.
111 Altogether, the characterisation of the murine retina suggests a possible relationship between the
112 relative density of Bruch's membrane's laminins and region-dependent RPE mechanical status.
113
114 **Laminin 511 density influences RPE phagocytic efficiency of photoreceptor outer segments.**
115 To dissect the hypothesis of a direct relation between biochemical cues from Bruch's membrane and
116 RPE mechanobiology, we established a bottom-up approach to scrutinize the role of the specific
117 laminin isoforms and their density gradient. Human induced pluripotent stem cell-derived RPE (hiPSC-
118 RPE) cells have already been successfully employed to model mature RPE and to study their
119 functionality [32,33]. Thus, we obtained RPE monolayers on polyacrylamide (PAA) hydrogels with 4 kPa
120 Young's modulus to best mimic Bruch's membrane stiffness. The gels were functionalised according
121 to Przybyla et al. [34] with specific concentrations of laminin, reaching saturation at a coating
122 concentration of around 20 µg/ml (Sup fig. 2G). The advantages of PAA gel as a culture substrate are
123 a defined stiffness (Youngs's modulus of the gel) and the protein-repellent nature of the polymer [35],
124 allowing control over the biochemical cues originating from the coating. Due to this reductionistic
125 approach, certain coating conditions were not permissive to obtain mature and intact RPE monolayers,
126 such as laminin 511 (composed by laminin α5, β1 and γ1) and collagen type IV alone or laminin 211
127 (composed by laminin α2, β1 and γ1) also in combination with collagen type IV (Sup. fig. 2 A - C).
128 Nevertheless, hiPSC-RPE cells adhere and form a mature monolayer when seeded on PAA gels coated
129 with different concentrations of laminin 332 and laminin 511, both in combination with collagen type
130 IV (Sup. Fig. 2 D). After a week of culture, hiPSC-RPE cells reach a low proliferative state and form a
131 thick polarised monolayer (~10 - 15 µm at the junctions) (Sup. fig. 3D), presenting apical microvilli as
132 shown by ezrin staining and scanning electron microscopy (Fig. 2 A – C). Furthermore, the staining for
133 fibronectin confirmed the absence of aberrant deposition of ECM proteins by the cells while cultured
134 (Sup. fig. 2 E).
135

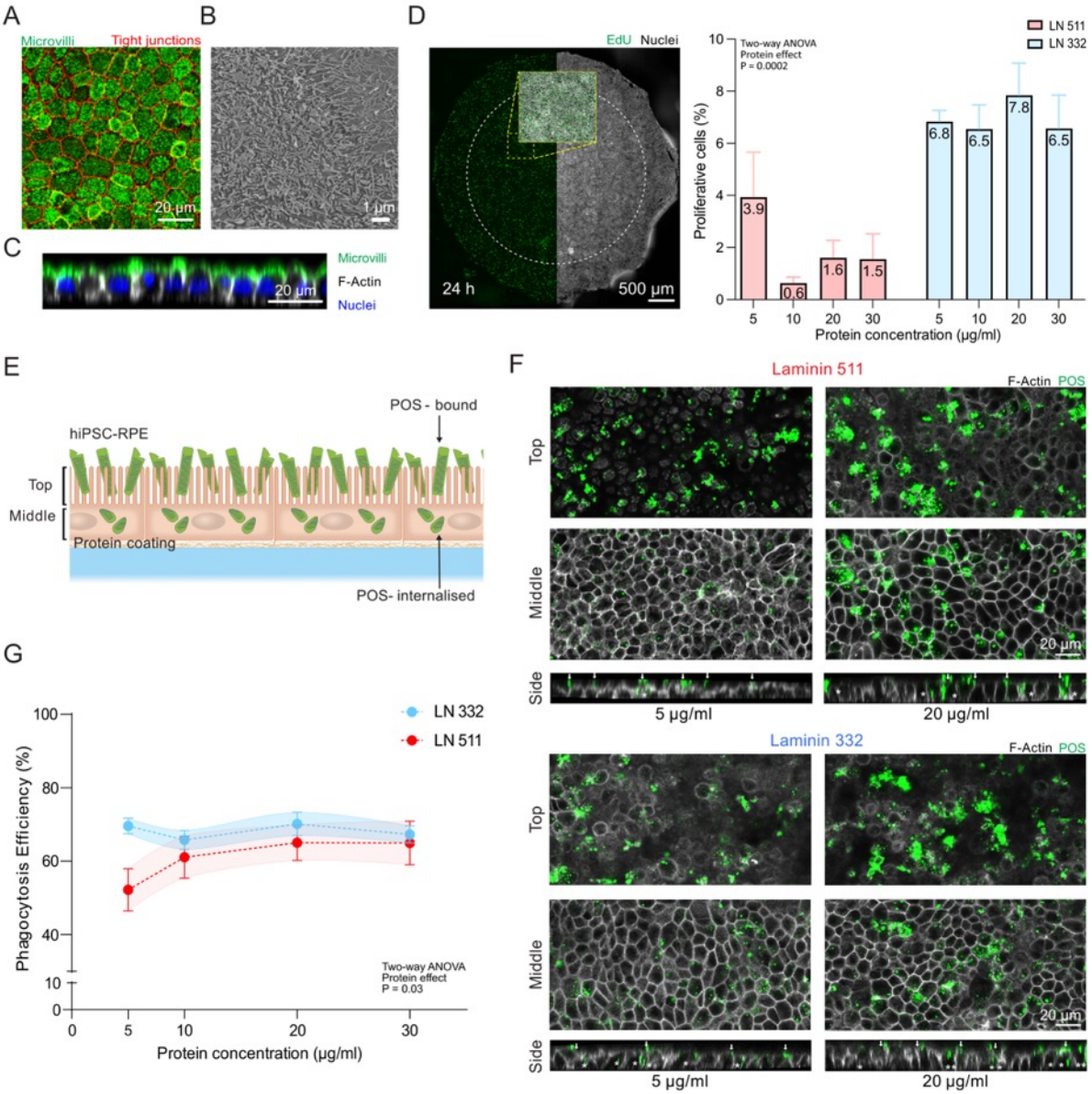

136

Figure 2: Human-relevant in vitro system for characterisation retinal mechanobiology. *hiPSC-derived RPE obtained on PAA gel with Young's modulus of 4 kPa coated with laminin 511 or laminin 332 in the presence of collagen type IV. After one week in culture, cells develop tight junctions (ZO-1) and apical microvilli (Ezrin) observed in a confocal cross section* ***(A)*** *and a scanning electron micrograph of the monolayer surface* ***(B)****.* ***(C)*** *Orthogonal projection of hiPSC-derived RPE epithelium displays a polarised monolayer with microvilli localised at the apical side of the cells.* ***(D)*** *Cellular proliferation rate within 24 h obtained using EdU labelling assay for cells cultured on the PAA gel surface. Representative picture of the gel overview indicates the number of proliferating cells within one gel (left). The ratio of nuclei with incorporated EdU (per cent of proliferative cells) was quantified by the fluorescent signal in the central region of the gel to avoid possible edge effects (white circle). The data show average values ± SEM from at least 4 independent experiments. Statistic was performed using a mixed-effects model (REML) with the Geisser-Greenhouse correction, Tuckey's multiple comparisons test.* ***(E)*** *Schematic representation of the photoreceptor outer segment internalisation assay on one-week-old RPE monolayer.* ***(F)*** *Representative confocal images of the hiPSC-RPE cells on PAA hydrogel with laminin 511 or laminin 332 coating (in the presence of collagen type IV). The top row indicates FITC-labelled POS fragments at the apical surface of the cells. The middle row represents an optical section of the cell monolayer with POS fragments inside. The results of the POS phagocytosis assay are visible in the orthogonal projections (bottom row) where arrows and stars indicate bound and internalised POS respectively.* ***(G)*** *Average phagocytosis efficiency ± SEM for different laminin isoforms and their coating conditions from at least 4 independent experiments. The phagocytosis efficiency is defined as the amount of internalised POS divided by total POS. Statistical significance was tested using a mixed-effects model (REML) with the Geisser-Greenhouse correction, Tuckey's multiple comparisons test.*

137 Considering that the observed *in vivo* density gradient of laminin α5 and 332 from the retinal centre
138 to the far periphery corresponds to the visual angle, we wondered if there is any direct relationship
139 between this density gradient and the ability of hiPSC-RPE to bind and phagocyte POS. Indeed, RPE
140 phagocytic load as a result of gradually changing photoreceptor density, naturally follows the visual
141 angle, decreasing from the centre towards the periphery [14]. Hence, we tested the ability of RPE
142 monolayers on PAA gels to bind and phagocyte POS fragments, which were isolated from porcine
143 eyes and fluorescently labelled with FITC (Fig. 2 E - G). The quantification shows that, overall, at high
144 laminin coating density (10 - 30 µg/ml) there is a comparable efficiency of phagocytosis between
145 laminin 332 and 511, whereas a divergence could be detected at the concentration of 5 µg/ml with
146 reduced efficiency of RPE on laminin 511 (~50 %) (Fig. 2 F, G).
147 In conclusion, hiPSC-RPE cells form a mature and functional monolayer on laminin 332 or 511 but not
148 on laminin 211 (with or without the addition of collagen type IV), excluding its major role in promoting
149 adhesion on Bruch's membrane for RPE. Furthermore, the phagocytosis assay revealed a reduction of
150 efficiency in internalising POS in RPE monolayers obtained with the lowest density of laminin 511.
151
152 **Laminin 511 density influences contractility levels in RPE monolayers.**
153 The quantification of RPE cell organisation and topological analyses in the retina suggested a direct
154 relationship between laminin density in the basement membrane and monolayer mechanical status.
155 Hence, following the logic of a comparative approach between *in vivo* and *in vitro* systems, we
156 performed morphometric and topological analyses of the monolayers obtained on the different laminin
157 isoforms and densities (Fig. 3 A - C, sup. fig. 3 A - C). The calculation of the average cellular area,
158 perimeter, elongation and neighbourhood expresses a stable relationship among all laminin densities
159 and isoforms, excluding their direct role in controlling monolayer topology. Nevertheless, we
160 wondered if those parameters may affect monolayer contractile forces. Hence, we used traction force
161 and monolayer stress microscopy to quantify RPE cell-matrix traction forces and cell-cell stresses in
162 different conditions (Fig. 3 D - G). The quantifications revealed an overall ability of laminin 511 to
163 promote higher traction forces compared to laminin 332 (Fig. 3 D, E). Interestingly, as observed for
164 the phagocytosis efficiency, the highest difference of average traction force (170 Pa vs 80 Pa) was
165 recorded at the lowest laminin density (5 µg/ml) (Fig. 3 E). Next, we used the information on the traction
166 forces and monolayer height (Sup. fig. 3 D) to calculate intercellular normal stresses at the different
167 conditions as previously shown [36,37] (Fig. 3D - G). Similarly, we observed a significant difference in the
168 overall monolayer absolute stresses at the lowest coating density of laminins (5 µg/ml) with an average
169 of ~1 Pa for laminin 511 and 0.6 Pa for laminin 332 (Fig. 3 G). As expected, the stress vectors exhibit
170 an average close to 0 Pa for both coatings and densities, indicating that monolayers are nearly in

171 equilibrium despite the variations in absolute contractility (Fig. 3 F). The difference in traction and
172 stress at the lowest laminin 511 density might be caused by a gradual increase in cell adhesion to
173 collagen type IV, which remained constant across the conditions. We therefore tested the effect of
174 collagen type IV on monolayer traction forces using laminin 332 as a control since laminin 511 alone
175 does not support the formation of a monolayer (Sup. fig. 2 A). The quantification shows an overall
176 decrease (~ 40%) of traction in the presence of collagen type IV (Sup. fig. 2 F), clearly excluding the
177 role of collagen type IV for the observed increased traction at the lowest laminin 511 density.
178 Moreover, the clear distinction in traction between laminin 511 and laminin 332 strengthens the
179 conclusion that the observed changes are exclusively laminin-induced.
180 Finally, we wanted to understand if the coating density could generally impact RPE cell surface
181 stiffness, which may affect POS adhesion and phagocytosis. Therefore, we performed nanoindentation
182 of RPE cells within the monolayers using a spherical probe of approximately 10 µm radius and
183 quantified the average Effective Young's modulus of the monolayers (Fig. 3 H). The data show that
184 RPE monolayers on laminin 511 are stiffer (~1.5 kPa) compared to laminin 332 (~1 kPa) regardless of
185 the protein surface density, thus excluding the effect of cellular stiffness for POS phagocytosis
186 efficiency.
187 In conclusion, the biomechanical characterisation of our model clearly indicates a divergent effect of
188 the low density of laminin 511 versus laminin 332 on the overall RPE mechanical balance promoting
189 an increased contractility of the monolayer.

190

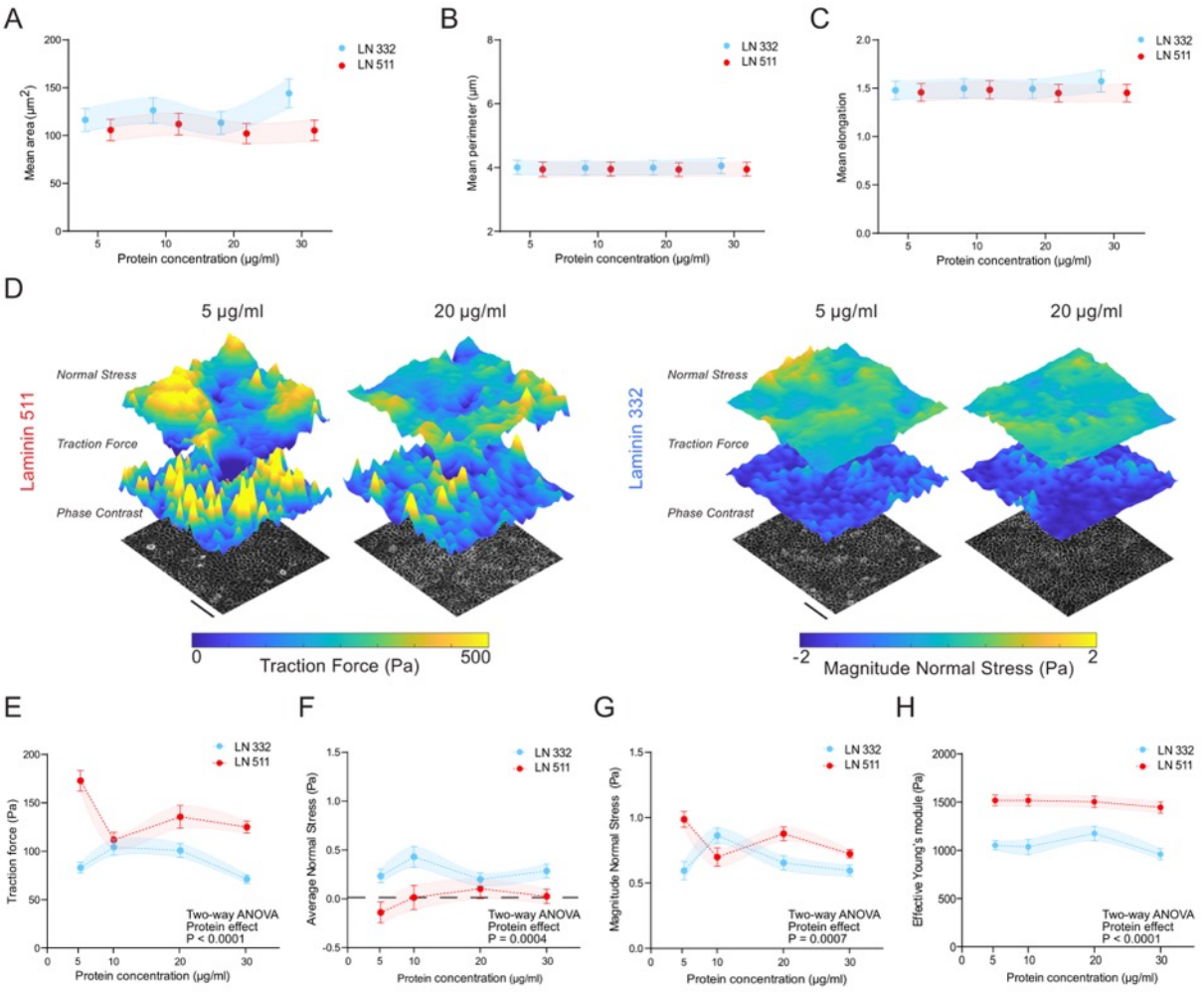

*Figure 3: **Laminin surface density affects the contractility of RPE monolayers.** The morphometric analysis reveals the absence of significant difference in cellular mean area **(A)**, mean perimeter **(B)** and mean elongation **(C)** between different laminin isoforms and densities from 3 independent experiments. **(D)** Representative traction force and monolayer stress profiles for different coating conditions and their quantifications **(E, F and G)** show a significant increase in contractility of RPE monolayers at the lowest laminin 511 density. **(H)** Quantification of the effective Young's modulus of the apical side of monolayer in different conditions. Data are shown as average ± SEM from at least 4 independent experiments. Statistical analyses were performed using a mixed-effects model (REML) with the Geisser-Greenhouse correction, Tuckey's multiple comparisons test.*

191 **Overall monolayer traction force modulates RPE functionality.**

192 Epithelial contractility levels have been shown to directly influence tissue functionality and reactivity [36–
193 43]. Thus, we asked ourselves whether the efficiency of RPE to phagocyte POS is generally affected by
194 the level of monolayer traction forces independently of the biochemical nature of ECM adhesion, i.e.,
195 laminin isoforms or density. To systematically adjust the traction force, we decided to tune either the
196 ECM physical cues (i.e., hydrogel stiffness) or the biochemical nature of adhesion (i.e., laminins vs
197 vitronectin) (Fig. 4 A). We then assessed the RPE efficiency in internalising POS by comparing it with
198 the maximum efficiency observed in RPE on laminins.

199 First, we obtained RPE monolayers on stiffer hydrogels (18 kPa) coated with laminin 511 or 332 (20
200 µg/ml) in the presence of collagen type IV (30 µg/ml), which developed a significantly increased
201 traction force compared to the one on 4kPa (~140 Pa and ~170 Pa respectively). This corresponded
202 to a reduced efficiency of these monolayers for POS internalisation (~ 40%) (Fig. 4 B - D left). Second,
203 we measured the phagocytic activity and traction forces of monolayers obtained on 4 kPa hydrogels
204 coated with a high concentration of vitronectin (250 µg/ml) to match the protein surface density of
205 laminins. Also in this case, the analyses revealed a higher average traction force (~ 200 Pa) which
206 corresponded to a reduced ability of RPE to internalise POS (~ 36%) (Fig. 4 B - D right).
207 To distinguish the exclusive role of cellular contractility from the possible converging effects of ECM
208 signalling, we inhibited or increased actomyosin contractility in RPE monolayers using a ROCK inhibitor
209 or a RhoA activator (Fig. 4 E - G). The reduction of contractility was performed on RPE monolayers
210 cultured on soft (4 kPa) surfaces coated with collagen type IV (30 µg/ml) with little addition of laminins
211 (2.5 µg/ml) which showed *per se* a low activity for POS phagocytosis (~ 50%). On the other hand, the
212 increase of contractility was induced in RPE on high-density laminins (20 µg/ml) in the presence of
213 collagen type IV. As expected, the drug treatments affected the ability of RPE to develop traction
214 forces with reduced traction after ROCK inhibitor treatment and increased after RhoA activation (Fig.
215 4 E, G top). Moreover, the quantification revealed a direct connection between actomyosin contractility
216 and monolayer efficiency in POS phagocytosis. Independently of the laminin type, RPE phagocytic
217 efficiency increased after ROCK inhibitor treatment (from ~50% to ~70%) and decreased after RhoA
218 activator treatment (from ~70% to ~50%) (Fig. 4 F, G bottom).
219 Overall, these data show the direct influence of RPE contractility on its ability to phagocyte POS.
220 Surprisingly, this effect is independent of the nature of adhesion and thus can be influenced by both
221 biochemical and physical ECM cues.
222
223
224
225
226
227
228

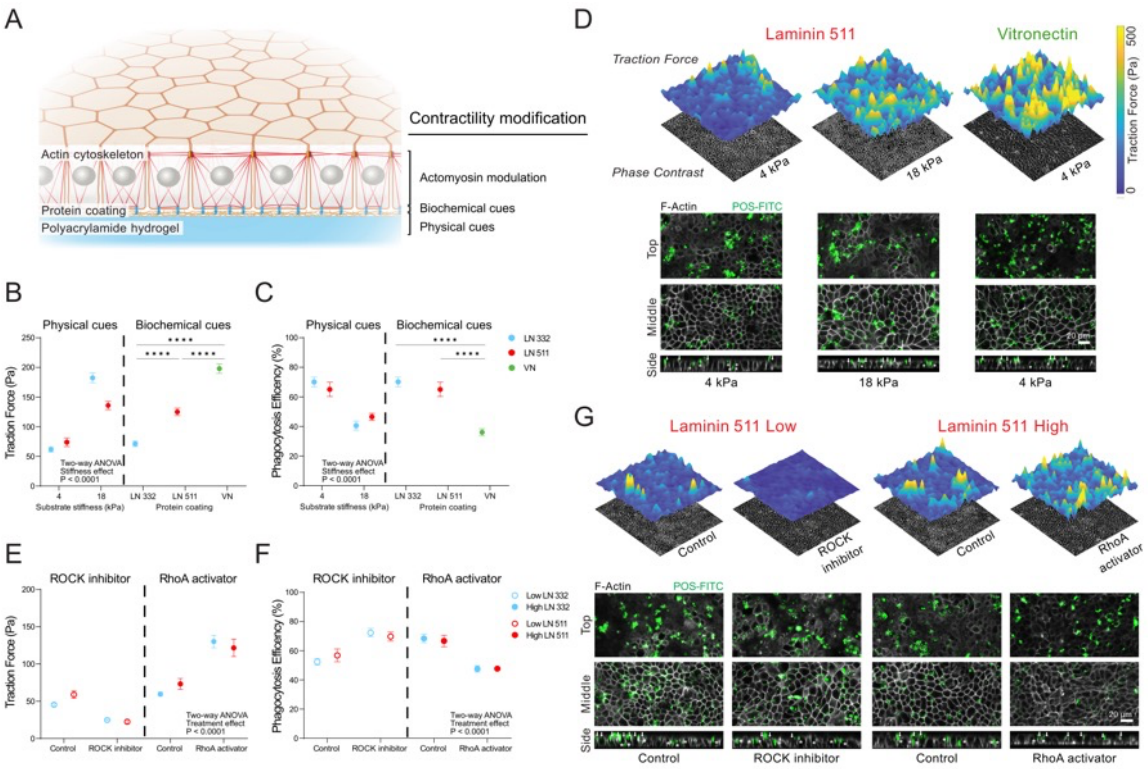

*Figure 4: Overall monolayer contractility modulates the cellular functionality. **(A)** Schematic representation of the experimental strategy to modulate monolayer contractility. Quantification of mean traction forces **(B)** and phagocytosis efficiency ±SEM **(C)** in RPE upon different ECM physical (stiffness) and biochemical cues (coating). **(D)** Representative traction force plots and immunofluorescent images of POS internalisation assay upon different physical or biochemical cues. PAA gels were coated with laminin 511 (LN 511) or laminin 332 (LN 332) (in the presence of collagen type IV) or with vitronectin (VN). ****p<0.0001 using mixed-effects model (REML) with the Geisser-Greenhouse correction, Tuckey's multiple comparisons test (physical cues) and Mann-Whitney test (biochemical cues). Drug treatment, affecting actomyosin contractility levels, using ROCK inhibitor and RhoA activator shows inverse dependence between the level of monolayer contractility (traction forces) **(E)** and its ability to phagocyte POS fragments **(F)**. Data are shown as mean ± SEM. ****p<0.0001 using mixed-effects model (REML) with the Geisser-Greenhouse correction, Tuckey's multiple comparisons paired test. **(G)** Representative traction force plots and immunofluorescent images of POS internalisation assay upon drug treatment.*

229

230 **Integrin β4/β1 ratio and keratin network organisation modulate RPE mechanical homeostasis.**

231 Epithelial cells in homeostasis mechanically couple their cytoskeleton to their basement membrane via
232 integrin receptors [5,44]. Intracellularly, integrin β1 subtypes interface with the actin cytoskeleton via talin,
233 whereas integrin α6β4 binds via plectin the keratin network[45]. Extracellularly, integrins β1 and β4 bind
234 with a redundant number of proteins, including laminins α3 and α5 chains [46,47]. Therefore, we
235 wondered why low densities of laminin 332 or 511 differently promote integrin-based adhesion in RPE,
236 thus influencing traction forces and consequent functional differences. Hence, we performed a
237 functional adhesion assay using blocking antibodies to address the engagement of specific integrin
238 subtypes on laminin-coated hydrogels (Fig. 5 A). Blocking the different beta chains (i.e., β1, β4, and
239 [αv] β3) resulted in a significant reduction of adhesion for β1 (LN 511 ~62% and LN332 ~75%) and no
240 significant effect in the case of β4 and αvβ3 integrins. In the presence of integrin β4 blocking antibody,

241 a tendency of reduction was observed on laminin 332. Hence, to avoid the effect of compensation by
242 β1 integrin, we concurrently blocked integrin β1 and β4, achieving nearly complete inhibition of RPE
243 cell adhesion onto low-density laminin 332 (~94%) with no significant drop on laminin 511 (Fig. 5 A,
244 left). A similar trend was also observed for integrin alpha chains, where a substantial reduction in
245 adhesion occurred upon combining integrin α6- and α3-blocking antibodies, suggesting the
246 predominant involvement of these two subtypes in adhesion process (Fig. 5 A, right).
247 Based on these findings, we stained target integrins on RPE cells detached from mature monolayers
248 and analysed their relative surface presence during adhesion to the low-density laminin via flow
249 cytometry (Fig. 5 B – E, sup. fig. 4). In line with the adhesion assay, the quantification revealed that
250 cells adhering to the low-density laminin 511 present a significantly higher level of β1 integrin on their
251 surface compared to cells adhering to laminin 332 (Fig. 5 B, C and supp. fig. 4 D). Instead, the levels
252 of β4, α3 and α6 integrins were comparable between low-density laminin 511 and 332 (Fig. 5 D and
253 sup. fig. 4 D - K). Furthermore, these results show that RPE cells adhering to low-density laminin 332
254 present a significantly higher ratio of integrin β4 to β1 compared to cells adhering to low-density
255 laminin 511 (Fig. 5 E).
256 Altogether, these data indicate the main role of integrins α6β1 and α3β1 to support the adhesion to
257 the low-density laminin 511 and integrins α6β1, α3β1, and α6β4 to low-density laminin 332.
258 The formation of hemidesmosomes has been shown to reduce cellular traction forces [48] and sensitivity
259 of nuclear mechanotransduction [49] via their role in nucleation and organization of the keratin
260 cytoskeleton [49,50]. Hence, encouraged by our *in vitro* findings, we were curious whether the different
261 laminin densities in Bruch's membrane presented different keratin network organisations. Using keratin
262 8-YFP knock-in mice [51] we imaged and segmented the different keratin networks in 3D using a recently
263 developed workflow [52] (Fig. 5 F - J). The analyses revealed that the keratin network gradually gets
264 thinner (reduced brightness) (Fig. 5 H), looser (higher segment length) (Fig. 5 I) and less bend (less
265 curved) (Fig. 5 J) from the centre to far periphery. This evidence supports the existence of a laminin-
266 defined mechanical balance in RPE which gradually shifts to a less prominent keratin contribution and
267 more contractile monolayer toward the retinal periphery (Fig. 6).

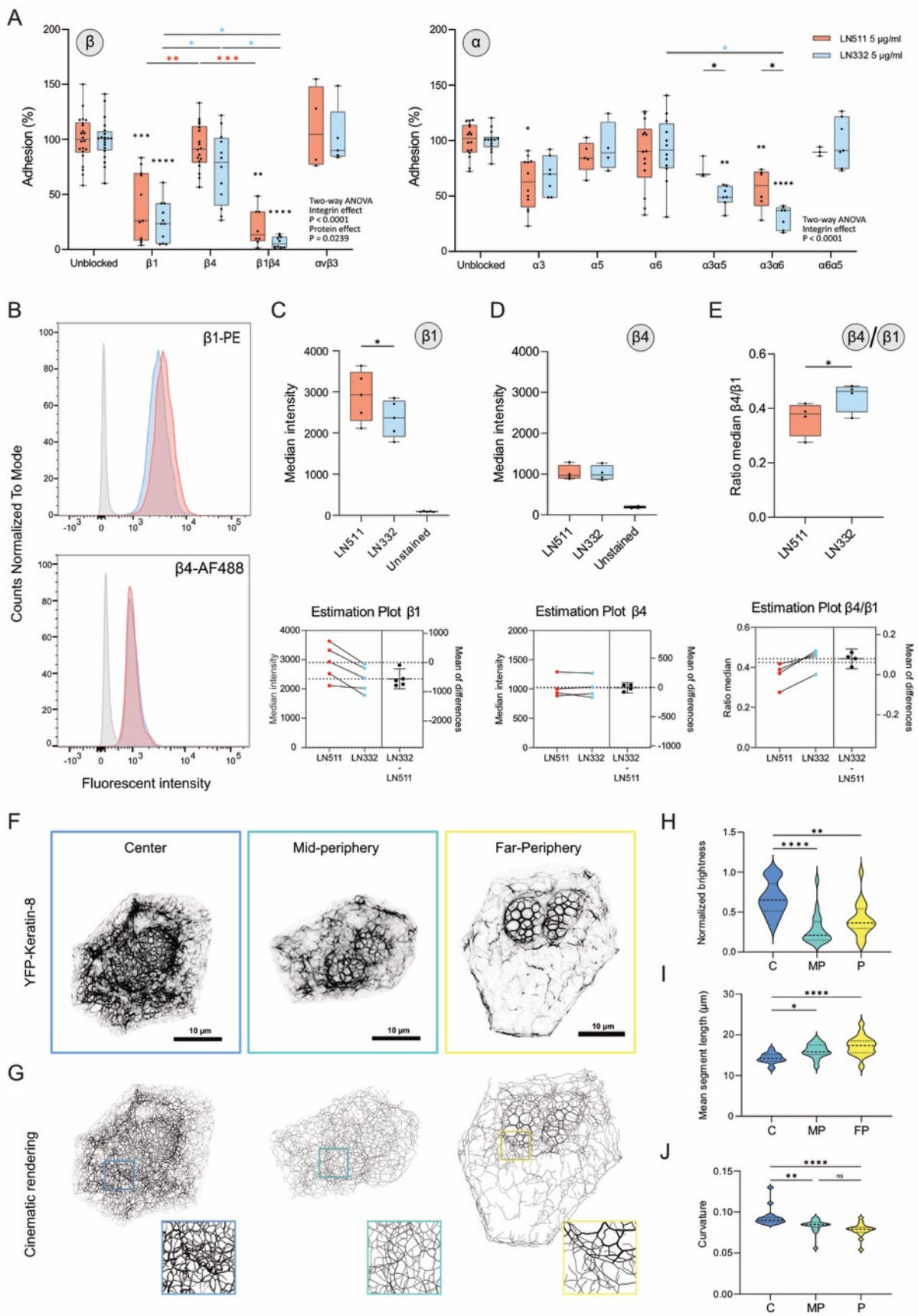
A
β
Adhesion (%)
Unblocked
β1
β4
β1β4
αvβ3
Two-way ANOVA
Integrin effect
P < 0.0001
Protein effect
P = 0.0239
α
LN511 5 µg/ml
LN332 5 µg/ml
α3
α5
α6
α3α5
α3α6
α6α5
Two-way ANOVA
Integrin effect
P < 0.0001
B
β1-PE
β4-AF488
Counts Normalized To Mode
Fluorescent intensity
C
β1
Median intensity
LN511
LN332
Unstained
Estimation Plot β1
Mean of differences
D
β4
Estimation Plot β4
E
β4/β1
Ratio median β4/β1
Ratio median
Estimation Plot β4/β1
F
Center
Mid-periphery
Far-Periphery
YFP-Keratin-8
10 µm
G
Cinematic rendering
H
Normalized brightness
C
MP
P
I
Mean segment length (µm)
FP
J
Curvature
ns

268

Figure 5: Laminin density defines RPE mechanical balance via integrin β4/β1 ratio and keratin cytoskeleton organization. ***(A)*** *Box and whisker plots of RPE cell adhesion percentage on low-density (5 µg/ml) laminin 332 or laminin 511-coated hydrogels, after incubation with integrin beta or alpha subunits blocking antibodies and control (cntr). * p < 0.05, ** p < 0.01, *** p < 0.001 ****p<0.0001 tested using a two-way ANOVA with Geisser-greenhouse and Tukey correction. Stars standing directly on the box and whisker show significance towards the control.* ***(B)*** *Representative flow cytometry histograms of the surface integrin β1 (top) and β4 (bottom) expression of RPE cell cultured for one week on low-density laminin 332 (light blue), laminin 511 (red), and unstained control (grey).* ***(C, D, E)*** *Box and whisker plots showing the distribution of intensity medians and the relative estimation plots from independent experiments for β1 and β4 integrins and their ratio. * p < 0.05 tested using paired t-test.* ***(F, G)*** *Representative images of RPE cells at different regions from YFP-keratin 8 mice and the resulting cinematic rendering of the keratin network.* ***(H, I, L)*** *Violin plots of normalized keratin brightness, mean segment length, and curvature in RPE from different retinal regions. * p < 0.05, ** p < 0.01 and ****p<0.0001 tested using a one-way ANOVA. Data are from three independent mice.*

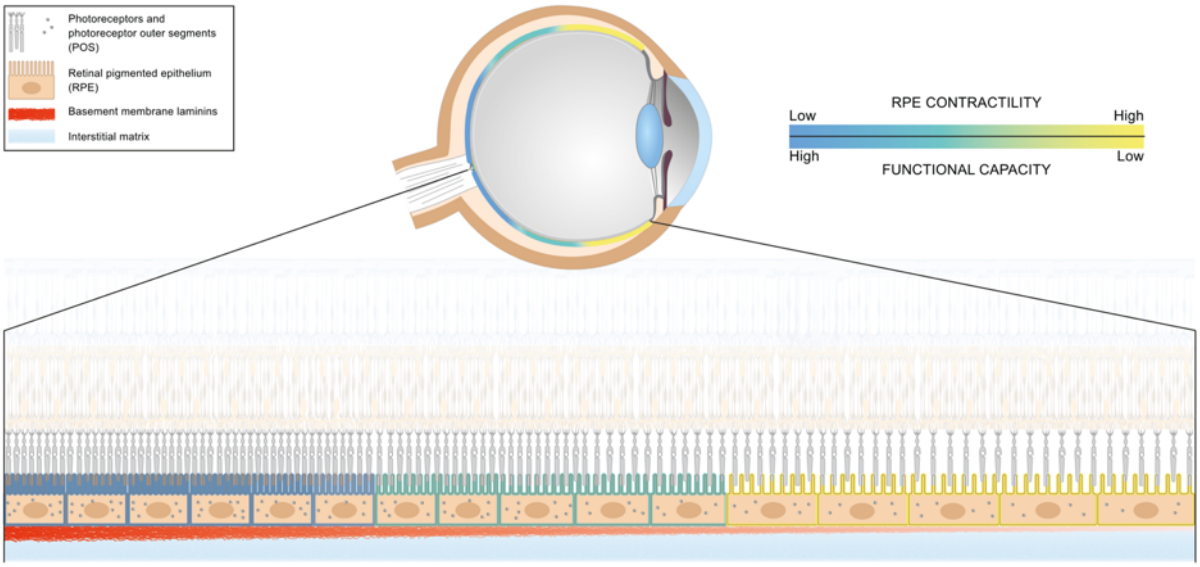

Figure 6: Schematic overview of RPE mechanical homeostasis. *The summary figure illustrates the ECM-orchestrated changes in the retinal tissue, focusing on the impact of decreasing basement membrane laminin density, altering RPE mechanics, and diminishing photoreceptor density, thus, functional load as we move towards the retinal periphery. The schematic highlights the laminin-defined mechanical balance within the RPE, demonstrating a gradual transition towards reduced functional capacity at the periphery. This visual representation brings together the key elements of the paper, providing a comprehensive overview of the dynamic interplay between laminin density, RPE contractility, and its functional load across the retinal landscape.*

DISCUSSION

Our findings demonstrate the unknown direct role of laminin density in regulating RPE functional capacity through epithelial contractility and, thus, its mechanical homeostasis. For the first time, we report the presence of a relative density gradient of specific laminin isoforms in the Bruch's membrane. Bruch's membrane has the highest laminin content at the retinal centre, whereas at the far periphery, the laminin 332 and α5-containing isoforms have the lowest density. This laminin density gradient correlates with a gradual increase in RPE cellular shape factor with the lower laminin density corresponding to more elongated cells. Furthermore, the topological analyses suggest a variation

280 along the visual axis. Cellular shape factor and cell-to-neighbourhood relationship directly correspond
281 to mechanical properties of the epithelial monolayers [20–22] and contractility [23,37,38]. Finally, the different
282 arrangements of the keratin network within the RPE imply that, towards the periphery, the actin
283 cytoskeleton has a more prominent contribution to the epithelial mechanical status. Altogether, this
284 evidence strongly indicates higher epithelial contractility at the far periphery compared to the centre.
285 Due to technical limitations for the direct *in vivo* quantification of mechanical properties and
286 contractility, we employed a complementary approach. Therefore, we established an *in vitro* model
287 using laminin-functionalized PAA gels and hiPSC-derived RPE cells. The stringent condition for ECM
288 availability and remodelling, created by the PAA gel, revealed a direct role of low-density laminin 511
289 in increasing RPE contractility (higher traction forces and monolayer stress) and reducing the epithelium
290 efficiency to phagocyte POS. Despite this increase in RPE contractility, there were no observed
291 alterations in cell shape or topology. This suggests that the monolayer topology and morphology *in*
292 *vivo* may be defined by the convergence of several factors. At the far periphery, RPE is anchored to
293 the ora serrata with complex intercellular connections [53]. In combination with monolayer contraction,
294 this possibly causes the observed topological variation. Moreover, our data rule out the exclusive role
295 of laminins in defining RPE monolayer organization or stiffness.
296 The effect of laminin α5 on cellular mechanics is not surprising. Laminin α5 containing isoforms have
297 been shown to enhance cell stiffness and support better shear stress mechanotransduction [54] and
298 intercellular tightness [55] in the endothelium. As shown for the epithelium, also RPE cells preferentially
299 adhere to this laminin by β1 integrins (i.e., α3β1 and α6β1 integrins). This is different from laminin 332,
300 which additionally supports RPE adhesion via α6β4 integrins, i.e., hemidesmosomes. The role of
301 hemidesmosomes in organizing the keratin network has long been recognised as crucial for the
302 mechanical integrity of epithelial tissues [56,57] and has been proposed to define their textile nature [44].
303 More recently, data from different labs have demonstrated that hemidesmosomes and the keratin
304 network reduce cellular traction force [48] and protect the nucleus from mechanical strain [49]. In agreement
305 with the tensegrity model, cellular mechanics is a balance of cytoskeleton-driven forces, where a
306 contractile actin cytoskeleton is counterbalanced by intermediate filaments [58–60]. Therefore, a higher
307 ratio of β4/ β1 integrins on RPE adhering to low-density laminin 332 could explain the quantified low
308 traction forces in contrast with low-density laminin 511, which promotes higher epithelial traction.
309 Similarly, a thinner and looser keratin network in RPE far periphery and elongated nuclei suggest a
310 higher contribution of the contractile actin cytoskeleton to tissue mechanics in this area. Nevertheless,
311 due to technical challenges, it remains an open question whether the relative amount of laminin
312 isoforms differ along the visual axis and whether the ratio between β4 integrins (hemidesmosomes)
313 and β1 integrins decreases with the distance from the optic nerve.

314 The fact that ECM density reduction increases epithelial traction has been previously proposed based
315 on the reduction of integrin β1 receptor engagement *in vitro* [36,61]. Here, for the first time, we show the
316 physiological relevance of this density and the importance of the β4/ β1 ratio for epithelial mechanics.
317 Future studies will need to focus on dissecting the relationship between laminin receptors' density and
318 their role in regulating epithelial mechanical homeostasis. This is particularly relevant for retinal ageing,
319 given the reported reduction in hemidesmosomal attachment sites in RPE [62].
320 A study on stem-cell derived RPE has previously shown that the organisation of the actin cytoskeleton
321 can predict the ability of differentiated cells to phagocyte POS [33]. Particularly, the presence of F-actin
322 stress fibres impaired the phagocytic activity of these cells. These data and our findings strongly
323 suggest that high contractility in RPE is detrimental to its homeostasis and function. RPE apical
324 microvilli interact with POS mostly via the Mer tyrosine kinase receptor (MerTK) and the integrin αvβ5
325 [63]. The activation of MerTK is thought to be involved in the inside-out activation of integrin αvβ5 with
326 the recruitment of talin, vinculin and interaction with F-actin [63]. These focal adhesion-like structures
327 have already been shown to mediate phagocytosis in macrophages and to be mechanosensitive [64].
328 Hence, the formation of this apical molecular clutch may be sensitive to the overall cellular contractility
329 defined by the ECM substrate and explains the lower efficiency of POS internalisation observed in this
330 work. Furthermore, the neural cell adhesion molecule (N-CAM) homophilic interaction between POS
331 and RPE may also be affected by increased RPE contractility affecting the bond lifetime, thus, binding
332 efficiency.
333 Overall, our work underlines the important role of RPE mechanobiology for outer retina physiology
334 and opens important questions about its role in retinal ageing. ECM remodelling while ageing may
335 affect cell adhesion and shift RPE mechanical homeostasis out of its optimal range, making it more
336 prone to phenotypical changes. Overcoming this threshold may cause sight-impairing diseases such
337 as (high) myopia and age-related macular degeneration. Moreover, the use of Rho kinase inhibitors,
338 as in glaucoma treatment [65,66], may be implemented to prevent the progression of RPE-specific
339 diseases. Undoubtedly, further studies will be necessary to elucidate to what extent RPE contractility
340 is involved in outer retina diseases.
341
342
343 CONTRIBUTIONS
344 J.D.R. conceived the project. A.N.K. and T.P. designed and performed all the experiments. I.D. and
345 F.S. helped in establishing hiPSC-derived RPE cell culture on PAA gels. F.S. supported the integrin
346 studies. T.Pr. supported image segmentations and analyses. T.H. performed and analysed AFM
347 experiments on decellularised Bruch's membrane. M.H. and A.S. contributed to morphometric

348 analyses and interpretation of RPE monolayers *in vivo* and *in vitro*. R.W. performed the segmentation
349 and analyses of the keratin network. R.L. provided keratin 8 - YFP mice and expertise on the keratin
350 network. J.D.R. and A.N.K. wrote the manuscript, and all authors discussed and commented on it.
351

352 ACKNOWLEDGMENT

353 This work was supported by a grant from the Interdisciplinary Centre for Clinical Research within the
354 Faculty of Medicine at the RWTH Aachen University and from the German Research Foundation - DFG
355 - (grant n° RU 337 2366/3-1). Furthermore, the authors acknowledge the support of the
356 Mechanobiology in Epithelial 3D Tissue Constructs (ME3T) graduate school (GRK 2415/363055819)
357 and the DWI – Leibniz-Institute for Interactive Materials. A.N.K is supported by the Add-on Fellowship
358 of the Joachim Herz Foundation. We acknowledge the help of the Flow Cytometry Facility, a core
359 facility of the Interdisciplinary Center for Clinical Research (IZKF) Aachen within the Faculty of Medicine
360 at RWTH Aachen University. We appreciate the technical support of Adam Breitscheidel in the graphic
361 design and Gloria's excellent help in imaging.
362

363 METHODS

364 **Retina flat mount preparation.** Retina flat mounts were prepared from BALB/c mice of 25-30 weeks
365 of age. After sacrifice, the eyes were enucleated and fixed with 2% (wt/vol) paraformaldehyde (PFA)
366 for 4 hours at 4°C rotating. To best visualize the RPE layer, the eyes were prepared as flat mounts
367 according to published protocol[67]. Briefly, the cornea, the iris and the lens were removed, and the
368 eyecup was cut into eight longitudinal slices to allow its spreading. Afterwards, the neurosensory retina
369 was gently detached exposing the RPE layer adhering to its ECM for fluorescent staining and imaging.
370 The animal care and sacrifice were conducted according to the German Animal Welfare Act (LANUV,
371 reference number 84- 02.04.2015.A190).
372

373 **Atomic force microscopy of Bruch's membrane.** Upon enucleation, murine eyes were freshly
374 dissected using cold phosphate-buffered saline without Ca^{2+} and Mg^{2+} ($PBS^{-/-}$) and containing protease
375 inhibitors as instructed by the manufacturer (Roche, 4693132001). Dissected eyes were denuded by
376 the RPE layer via incubation of the tissue for 60 minutes with 50 mM Tris–HCl buffer plus 20 mM
377 ethylenediamine tetraacetic acid (EDTA), pH 7.4, followed by 20 minutes incubation in 50 mM Tris–
378 HCl buffer and two washes of 10 minutes with 1 M NaCl, pH 7.4. Each solution contained freshly added
379 cOmplete™, EDTA-free Protease Inhibitor Cocktail (Roche, 4693132001). Next, the prepared eyes
380 were glued to a surface using Corning Cell-Tak Cell and Tissue Adhesive (Corning, 354240).
381 Cantilevers with a spherical colloidal tip of 6.62 µm diameter (Nano and More GmbH, CP-PNPS-SiO-

382 C-5) were used to indent 200 nm into the decellularised Bruch's membrane in different regions of the
383 eye. The experiments were performed in a Dimension Icon atomic force microscope (Bruker Co. USA).
384 Probes were calibrated using the thermal oscillation method, built into the software (Nanoscope 9.4).
385 Force distance curves were recorded with an approach and retraction speed of 1 µm/s, with a relative
386 maximal force set typically to 2 nN. The maximal range of the Z-piezo was set to 2.5 µm. All curves
387 were exported to ASCII files with the analysis software of the instrument. The approach part of the
388 curves was analysed using a custom-written script in Python (https://www.python.org) using the Hertz
389 model (equation (1)). The Poisson ratio was assumed to be v = 0.3. The last 40-50% of the data points
390 are fit to a line and subtracted as background.
391
392 $$F(\delta) = \frac{4}{3}\frac{E}{1-\nu^2}\sqrt{R}(\delta - \delta_0)^{3/2} \qquad (1)$$
393
394 The model fits the whole curve using a nonlinear fit (leastsq) from Scipy (https://www.scipy.org) finding
395 both Young's modulus and the contact point.
396
397 **Immunofluorescence of retinal tissue.** Fluorescent staining of retina flat mounts was performed as
398 follows. After fixation and dissection, the tissue was incubated for one hour in 1% bovine serum
399 albumin (BSA) (wt/vol) in $PBS^{-/-}$ containing 0.1% (vol/vol) Triton X-100, followed by overnight staining
400 at 4°C with primary antibodies or phalloidin dissolved in $PBS^{-/-}$ solution of 1% (wt/vol) BSA and 0.1%
401 (vol/vol) Triton X-100. Secondary antibodies were diluted in $PBS^{-/-}$-containing 0.1% (vol/vol) Triton X-
402 100 and incubated with the tissue at room temperature for two hours. Finally, the retinas were
403 incubated for 15 minutes with 5 µg/ml Hoechst 33342 (Thermo-Fischer Scientific, 62249) in $PBS^{-/-}$
404 before being mounted on glass slides with Mowiol mounting medium (Sigma-Aldrich). Primary and
405 secondary antibodies used in this work are listed in supplementary table 1.
406
407 **Retinal extracellular matrix quantification.** To quantify the relative amount of ECM protein in the
408 Bruch's membrane upon immunofluorescence staining, Z-stacks (0.5 µm optical slices) from the
409 different regions were obtained using a Zeiss LSM 710 (Carl Zeiss) confocal microscope using unified
410 illumination settings. The distance from the optic nerve was monitored using the automated stage of
411 the microscope and setting the optic nerve as an origin. Within the eye, Z-stacks for each region were
412 recorded per eight longitudinal slices, respectively. Mean fluorescent intensity in single optical sections
413 identified as BrM was measured using Fiji software (National Institutes of Health, USA). Manually
414 defined regions of interest (ROIs) were selected to avoid artefacts due to tissue tearing during

415 preparation (Fig. 1 I "stars"). Three to five ROIs were measured for each stack, and the fluorescence
416 intensity of all data was normalized to the highest measured value in the eye.
417
418 **Keratin-8 network segmentation and characterization.** Retinas for keratin-8 analysis were prepared
419 as flat mounts from homozygous keratin 8-YFP knock-in mice [51]. In each region (centre, mid periphery
420 and far periphery), z-stacks of six cells were recorded per animal using the Airyscan mode at a Zeiss
421 LSM 710 (Carl Zeiss), for a total of 54 analysed cells. To ensure the analysis of only individual cells, the
422 signal within individual cells was cropped from confluent monolayers using standard tools in Fiji. Cell
423 borders were manually defined for each z-slice and the cell exterior was set to a grey value of 0. The
424 obtained images were segmented and processed to obtain a keratin network model for each cell as
425 previously described [52] Finally, custom-made Matlab scripts were used to analyse the network
426 properties including brightness, segment length and curvature [52].
427
428 **hiPSC-RPE culture.** Differentiated hiPSC-RPE were purchased cryopreserved from FUJIFILM Cellular
429 Dynamics and after thawing, seeded in 24-well plates coated with 2.5 µg/ml Vitronectin XF (StemCell
430 Technologies, 07180) at a density of 1600-1800 cells/mm^2. Cells were cultured to confluence in a
431 humidified incubator at 37°C and 5% CO_2 and then, after detachment, reconstituted in
432 CELLBANKER 2® freezing media (Amsbio LLC, 11891) and kept in liquid nitrogen for future use. Cell
433 detachment for cryopreservation or experiments was achieved through 30 minutes of incubation with
434 5 mM EDTA in PBS without Ca^{+2} and Mg^{+2} ($PBS^{-/-}$) followed by TrypLE Express dissociation agent
435 (Gibco, 12605-010) for five minutes at 37°C. Prior to seeding, cells were centrifuged at 300 g for 5
436 minutes and resuspended in the media at the desired density. For the experiments, cells were thawed
437 again and cultured for up to two weeks until confluence before use. For seeding on polyacrylamide
438 hydrogels, cells were seeded at a density of 5000-6000 cells/mm^2, corresponding to the RPE density
439 in the human macula [15] and cultured for one week. Cells were cultured in hiPSC-RPE medium
440 composed of MEM α (Thermo Fisher, 12549-089), 5% (vol/vol) knock-out serum replacement (Gibco,
441 10828-028), 1% (vol/vol) N-2 supplement (Gibco, 17502-048), 55 nM hydrocortisone (Sigma-Aldrich,
442 H6909), 250 µg/ml taurine (Sigma, T0625), 14 pg/ml triiodo-L-thyronine (Sigma, T5516) and 25 µg/ml
443 gentamicin (Gibco, 15750-060). The medium was exchanged every second day.
444
445 **Hydrogel preparation and functionalisation.** To obtain flat hydrogel substrates, a mixture of 40%
446 acrylamide (Bio-Rad, 1610140) and 2% bis-acrylamide (Bio-Rad, 1610142) in distilled water was first
447 prepared. The following ratios of acrylamide / bis-acrylamide in the mixture were used to reach
448 different hydrogel Young's moduli quantified by nanoindentation: 5 % / 0.1 % (wt/vol) for 4 kPa and

449 10% / 0.07 % (wt /vol) for 18 kPa. Then, the mixture was combined with 0.5 % of (vol/vol) ammonium
450 persulfate (Sigma Aldrich, 248614, 10 % (wt/vol) stock solution in distilled water) and 0.05 % (vol/vol)
451 N`-tetramethylethylenediamine (TEMED) (Sigma Aldrich, 411019), and pipetted between
452 glutaraldehyde-activated glass bottom petri dishes (Cellvis, D35-20-0-N) and a hydrophobic glass
453 coverslip. If hydrogels were used for traction force microscopy, 1 µm yellow-green carboxylate-
454 modified polystyrene microbeads (Sigma, L4655) were included in the solution.
455 ECM proteins were crosslinked on the hydrogels' surface according to the protocol described by
456 Przybyla L. and colleagues [34]. Briefly, for functionalisation solution, we prepared stocks of 0.5 M HEPES
457 NaOH pH6 and 0.2% (wt/vol) bis-acrylamide in distilled water, 0.2 % (vol/vol) tetramethacrylate (Sigma,
458 408360) and 3% (wt/vol) hydroxy-4'-(2-hydroxyethoxy)-2-methylpropiophenone (Sigma, 410896) in
459 ethanol. Acrylic acid N-hydroxysuccinimide ester (Sigma, A8060) was initially dissolved in DMSO (10
460 mg/ml) and later reconstituted in 50% ethanol for the final concentration of 0.03 % (wt/vol). Calculating
461 0.5 ml solution per gel, we combined 216.65 µl of sterile water, 50 µl of 0.5 M HEPES NaOH pH 6,
462 32.5 µl of ethanol and 25 µl of bis-acrylamide and degassed under vacuum for 20 min. Then, 5 µl
463 tetramethacrylate, 4.165 µl hydroxy-4'-(2-hydroxyethoxy)-2-methylpropiophenone and 5 µl of ester in
464 161.65 µl of 50% ethanol were added to the degassed solution. The completed functionalization
465 solution was applied over the surface of hydrogels, previously partly dehydrated in a 70% ethanol
466 solution for 5 minutes, and the hydrogels were exposed for 10 minutes to ultraviolet light. After
467 sequential double washing with 25 mM HEPES buffer and $PBS^{-/-}$ for a total of 20 minutes, the gel
468 surface was incubated overnight at 4°C with the desired ECM protein solution. Human recombinant
469 laminin-511 (Biolamina, LN511-0202) and laminin-332 (Biolamina, LN332-0202) were prepared at the
470 desired concentration in PBS containing Ca^{2+} and Mg^{2+} ($PBS^{+/+}$) mixed with 30 µg/ml collagen type IV
471 (Sigma-Aldrich, M7027-100G). Vitronectin (StemCell Technologies, 07180) was used without dilution
472 at 250 µg/ml. Finally, the obtained hydrogels were sterilized by 30 min ultraviolet light irradiation
473 before their application as cell culture substrates.
474 To represent surface protein saturation, gels were chemically crosslinked and coated with laminin-511
475 at concentrations of 5, 10, 20 or 30 µg/ml along with collagen type IV (30 µg/ml) in $PBS^{+/+}$. After
476 overnight incubation at 4°C, gels were thoroughly washed with $PBS^{+/+}$ to remove unbound protein,
477 fixed with 2% PFA for 10 minutes at room temperature, blocked with 1% BSA and stained with primary
478 Anti-mouse laminin α5 (gift from Lydia Sorokin) and secondary Anti-mouse IgG AF594 (Invitrogen,
479 A11005). Between all steps, gels were washed with $PBS^{-/-}$ for at least 1h. Stained gels were imaged
480 with a 63x objective on ApoTome.2 Fluorescence Microscope (Carl Zeiss), with at least 10 regions per
481 gel. The average intensity of each image was measured using Fiji software, and the final results were
482 plotted in GraphPad Prism 10.

483

484 **Immunofluorescence staining of hiPSC-RPE.** Cells on hydrogels were first quickly washed with warm
485 (~37 °C) $PBS^{+/+}$ then fixed with warm (~37 °C) 2% (wt/vol) PFA for 8 minutes at room temperature.
486 After fixation, cells were permeabilized with 0.3% (vol/vol) Triton X-100 for 2 minutes and blocked with
487 1% (wt/vol) BSA for 30 minutes at room temperature. Primary antibodies or Phalloidin-iFluor 647
488 Reagent (Abcam, ab176759) in PBS containing 1% (wt/vol) BSA were incubated overnight at 4°C. The
489 following day, secondary antibodies were diluted in a PBS solution containing DAPI (1 µg/ml,
490 Invitrogen D1306) and incubated with the sample for 30 minutes at room temperature. Primary and
491 secondary antibodies used in this work are listed in supplementary table 1. The samples were imaged
492 in PBS solution to match the immersion type of the objective. Both stained retinas and cells were
493 imaged using Plan-Apochromat 40x water immersion objective on Zeiss LSM 710 confocal microscope
494 with Airyscan capability (Carl Zeiss).

495

496 **Live staining.** For live imaging of F-actin, hiPSC-RPE cells cultured on PAA gels were incubated with
497 500 nM of a fluorogenic F-actin probe SirActin (Spirochrome, SC001) containing medium for at least
498 two hours before imaging. The samples were imaged using Plan-Apochromat 40x water immersion
499 objective on Zeiss LSM 710 confocal microscope with Airyscan capability (Carl Zeiss). Orthogonal views
500 from Z-stacks acquired via confocal live-imaging of F-actin (SirActin) were used to measure the average
501 junctional height of cultured RPE monolayers using Fiji image processing package (National Institutes
502 of Health, USA).

503

504 **Morphometric and topology analyses.** Microscopy images of RPE *in vivo* and *in vitro* were segmented
505 using the cellpose software [68] (www.cellpose.org) applied on F-Actin micrographs. Segmented cells
506 were imported into Fiji as ROIs and used to generate skeletonised images. The skeletonised images
507 were then imported into custom-written MATLAB software [69]. Prior to analysis, the software removes
508 15 pixels on the sides of the images to remove poor mask definition by cellpose (Sup. fig. 1 B), and
509 then applies a Gaussian filter with a standard deviation of 2 pixels (function "imgaussfilt") to correct
510 the pixel connectivity on the masks provided by cellpose. Finally, the software extracts information
511 about the cell morphology (cell area, perimeter, and elongation) and topology (cell neighbours) as
512 previously described [69]. For these analyses, the cells at the edge of the picture were not considered to
513 avoid any segmentation error (Sup. fig. 1 C). For *in vivo* images, in total, 24 images from 3 different
514 mice have been analysed for the "centre" and "mid periphery" regions of the retina (8 images each)
515 and 23 images for the "far periphery" region (8-8-7 images for the 3 mice respectively). This
516 corresponds to a total cell number of 5575 cells for the centre, 7957 for the mid periphery and 7863

517 for the far periphery. For *in vitro* images, 71 images were analysed (at least 2 images per experiment).
518 Each image provided in between 86 and 312 cells. Because of segmentation error, to remove
519 unnaturally large cells, cells with a rescaled area (see below) higher than 2, and cells with a
520 neighbourhood larger than 10 cells have been removed from the analysis. The number of cells per
521 condition is summarised in supplementary table 2. To build both Lewis' and Desh' law, data were
522 separated with respect to their number of neighbours and binned in different classes before being
523 averaged. To build Aboav-Weaire's law, the cells at the images' edge were removed, since their
524 neighbourhood is not defined. For that, the neighbourhood of each cell is reconstructed to determine
525 the average position of the collection of neighbours. If the distance between their average position
526 and the central cells is less than 30 px, the central cell is assumed to be in the bulk of the image and
527 not on the border of the image. To plot Aboav-Weaire's law, we computed b(n) defined in (2).
528
529 $$b(n) = (n-6)\mu_{m(n)} - \sigma_n^2 \qquad (2)$$
530 where $\mu_{m(n)}$ is the mean size of the neighbourhood among the neighbours, and σ_n^2 is the central second
531 moment of the distribution of neighbours, i.e., its variance. Such distribution is taken for a given mouse,
532 not among different mice. Data from the different mice are average together with a ponderation
533 proportional to the total number of cells making the statistics.
534
535 **Scanning Electron Microscopy** (Critical Point Drying). After a week in culture on a polyacrylamide gel
536 with the defined coating, hiPSC-RPE were fixed in 3% glutaraldehyde (Agar scientific, Wetzlar,
537 Germany) for 4 h at 4°C followed by a washing in 0.1 M Soerensen's Phosphate Buffer (Merck,
538 Darmstadt, Germany). The dehydrating step was performed in the ascending alcohol series with 10
539 minutes duration each. The samples were sequentially immersed in the following solutions: 30%
540 ethanol, 50% ethanol, 70% ethanol, 90% ethanol, and three times in 100% ethanol. Critical Point
541 Drying was performed in liquid CO2. Prior to imaging, cell monolayers were coated with 10 nm
542 gold/palladium layer.
543
544 **Proliferation assay.** Levels of proliferation in hiPSC-RPE monolayers were assessed using a
545 proliferation assay kit Click-iT EdU (Thermo Fisher, C10337). Cells were incubated with a 1:1 mixture
546 of cell culture supernatant and 5-Ethinyl-2'-Desoxyuridin (EdU) (20 µM) containing hiPSC-RPE cell
547 culture medium for 24 h. Final EdU concentration in the mixture was 10 µM. Afterwards, cells were
548 fixed as described for immunofluorescent labelling and processed according to the manufacturer's
549 instructions. As EdU incorporates into newly synthesized DNA, proliferating cells were identified as
550 having their nucleus positively stained with EdU-Alexa Fluor 488. The total area of the gel was imaged

551 on Axio Observer 7 (Carl Zeiss) microscope as an overview using the tiles option. The ratio of
552 proliferating cells was calculated in comparison with DAPI-positive nuclei and quantified using the
553 particle analysis plugin of Fiji software (National Institutes of Health, USA).
554
555 **Photoreceptor outer segment internalisation assay**. Photoreceptor outer segments (POS) were
556 isolated in batches from porcine eyes from a local slaughterhouse as previously described [70]. Briefly,
557 the eyes were dissected using a red safelight lamp as the only illumination source, and the neural retina
558 was collected. After retinal mechanical homogenisation, POS were isolated via ultracentrifugation in a
559 sucrose gradient. Thereafter, POS were labelled with 2.5 mg/ml FITC dye (Thermo Fisher, F1906),
560 resuspended in DMEM (Thermo Fisher, 31331-028) containing 2.5% sucrose and stored in aliquots at
561 -80 °C for future use. For internalisation assay, POS aliquots were thawed in a water bath, washed with
562 medium, centrifuged at 2300g for 5 min and resuspended in hiPSC-RPE cell medium to an amount of
563 roughly 10 POS per RPE cell in culture. Human MGF-E8 protein (R&D Systems, 2767-MF-050) and
564 human protein-S (Coachrom, pp012A) were added at respectively 2.4 µg/ml and 2 µg/ml to aid the
565 internalisation. Next, hiPSC-RPE monolayers were washed twice with warm media and incubated for
566 four hours at 37°C with the prepared mixture at a density of approximately ten POS per cell. After
567 incubation, the monolayers were gently washed four times with warm $PBS^{+/+}$ and fixed for fluorescence
568 staining as described. Phagocytosis efficiency was calculated as projected area of internalised POS
569 divided by the total projected POS area in the same field of view. Internalised POS were identified in
570 orthogonal views from confocal optical sections (0.5 µm) by using F-actin staining to distinguish
571 between apical-bound and internalised segments. Analyses were automatised with the particle
572 analyses plugin of Fiji software (National Institutes of Health, USA) after applying a binary mask on the
573 images.
574
575 **Traction force and monolayer stress microscopy.** Traction force quantification and monolayer stress
576 calculations were performed as previously described [36,37]. Briefly, a week-old monolayer cultured on a
577 PAA gel substrate containing fluorescent beads was imaged using Axio Observer 7 (Carl Zeiss)
578 microscope for the beads signal. Then, the monolayer was detached with 0.5% SDS solution in $PBS^{-/-}$
579 followed by washing steps and 20 minutes of gel incubation in cell media to prevent gel shrinkage due
580 to the solvent change. The positions of the fluorescent beads in the hydrogel after the cell detachment
581 (relaxed state of the gel) were compared with the tense gel before, and beads displacement vectors
582 were calculated using the particle image velocimetry (PIV) plugin of Fiji (National Institutes of Health,
583 USA). Traction forces were calculated from these vectors using the Fourier transform traction cytometry
584 plugin (FTTC) of Fiji (National Institutes of Health, USA). Next, based on the traction force information,

585 average normal stress vectors were calculated using a force balance algorithm in MATLAB (MathWorks)
586 as formulated elsewhere [36,37]. For each measured sample, the average cell height was calculated using
587 a live actin staining (SirActin, Spirochrome) to correctly input the force balance algorithm.
588
589 **Stiffness measurements of hiPSC-RPE monolayers.** Measurements were performed using a Chiaro
590 Nanoindenter System (Optics 11 Life) mounted on Zeiss Axio Observer 7 (Carl Zeiss) with an
591 environmental chamber sustaining 37°C. A probe of 10 µm radius and 0.025 N/m stiffness (Optics 11
592 Life) was used and the indentation was performed in Displacement control mode, indenting 10 µm
593 into the cells monolayer. Approach curves were fitted via the DataViewer V2.4.0 software (Optics 11
594 Life) using a Hertzian contact model according to a set indentation depth from 0 to 3 µm for the apical
595 stiffness. A Poisson's ratio of 0.5 was used and a maximum load of 30% was allowed for setting the
596 contact point. Only results from well fitted data ($R^2 > 0.95$) were considered for statistics.
597
598 **Drug experiments.** For activation of the RhoA-dependent pathways, we incubated RPE monolayers
599 with Rho activator II (Cytoskeleton, CN03-A) and Rho kinase (ROCK) inhibitor Y-27632 (Sigma Aldrich,
600 Y0503) (https://doi.org/10.3390/cells10081927). Briefly, the one-week-old RPE monolayers on a
601 hydrogel coated with high laminin density (20 µg/ml) were treated with Rho activator II (1 µg/ml)
602 containing media for 3 hours prior to POS phagocytosis assay or traction force measurements to
603 promote the actomyosin contractility, or with an equal volume of water as a solvent control. To reduce
604 the actomyosin contractility at low laminin surface density (2.5 µg/ml), ROCK inhibitor (25 µM) was
605 added to the media one hour prior the POS phagocytosis assay or traction force measurements. An
606 equal volume of DMSO was used as a solvent control. Further analysis was performed as described in
607 the relevant chapters.
608
609 **Adhesion assay.** For cell adhesion assay, a confluent monolayer of hiPSC-RPE cells cultured in a 24-
610 well plate was detached with 30 minutes incubation of 750µl of 5 mM EDTA in $PBS^{-/-}$ without enzymatic
611 treatment to prevent unwanted receptor cleavage. Cells were gently washed with an additional 750 µl
612 of EDTA in $PBS^{-/-}$ and the whole solution was transferred into the 15 ml Falcon tube. After cell counting,
613 the suspension was centrifuged at 300 g for 5 minutes. The pellet was resuspended in ice-cold media
614 in half the volume required for the experiment and transferred to low protein binding tubes. Ice-cold
615 media should contain 20 µg/ml blocking antibody for blocking experiments. After 15 minutes of
616 incubation on ice, the cell suspension was diluted (1:2) with the equivalent volume of warm media and
617 immediately transferred onto the hydrogel surface. After 15 minutes at 37°C and 5% CO_2, hydrogel
618 surfaces were gently washed with warm $PBS^{+/+}$ to remove not attached cells, fixed with 2% PFA at

619 room temperature for 8 minutes, and stained for F-Actin (Phalloidin-iFluor 488 Reagent, Abcam -
620 ab176753) for analysis. The number of attached cells was quantified using the particle analysis plugin
621 in Fiji software and normalised to the mean of control samples to convert as a percentage of adhesion.
622 The following azide-free blocking antibodies were used: integrin β1 (clone P5D2) (Santa Cruz, sc-13590
623 L), integrin β4 (clone ASC-8) (Merk, MAB2059Z), integrin αvβ3 (clone LM609) (Merk, MAB1976Z),
624 integrin α3 (clone P1B5) (Merk, MAB1952Z), integrin α5 (clone P1D6) (Merk, MAB1956Z), integrin α6
625 (clone GOH3) (Santa Cruz, sc-19622 L).
626
627 **Flow cytometry.** One-week-old hiPSC-RPE cells were carefully detached from the hydrogel substrate
628 by incubation with 10 mM EDTA in $PBS^{-/-}$ at 37°C and 5% CO_2 for 30 minutes, followed by Accutase
629 solution (Sigma Aldrich, A6964) for 15 minutes. During this period, gentle shaking was beneficial for
630 detachment. Cells were gently washed from the surface with an additional 1 ml of EDTA in $PBS^{-/-}$,
631 transferred into the 15 ml tube and centrifuged for 5 minutes at 300 g. After centrifugation, cells were
632 dispersed in ice-cold $PBS^{-/-}$ and divided into two separate tubes: one will contain the whole antibody
633 panel, and another will be stained for β4 integrin alone. For the first tube, the viability staining with
634 LIVE/DEAD™ Fixable Near IR(780) Viability Kit (Thermo Fisher Scientific, L34992) was performed
635 during the 15-minute incubation on ice protected from the light. After centrifugation at 300 g for 4
636 minutes, cells were fixed with 1 ml of 1% PFA for 5 minutes on ice and resuspended in 100 µl of $PBS^{-/-}$
637 containing 3% BSA and 5 mM EDTA (FACS buffer) for 6 minutes centrifugation at 300 g. Fluorescently
638 conjugated antibodies (see table 1) were added according to the manufacturer's instructions and
639 incubated with cells for 45 minutes on ice protected from the light. After washing, cells were
640 resuspended in 400 µl of the FACS buffer and filtered using the Flowmi(R) Cell Strainer (MERK,
641 BAH136800040) directly into the flow cytometry tube for the measurements. Stained cells were
642 analysed using a BD LSRFortessa flow cytometer equipped with 405, 488, 561 and 640 nm lasers.
643 Analysis of the data was carried out using the FlowJo software.
644
645 **Statistics.** Statistical analysis was performed using Prism (GraphPad). Data were tested for normality
646 before proceeding to further statistical analyses. Sample conditions and the specific test used for
647 each data set are indicated in corresponding figure captions.

648 REFERENCES

649 1. Anlaş, A. A. & Nelson, C. M. Tissue mechanics regulates form, function, and dysfunction. *Curr Opin Cell Biol*
650 **54**, 98–105 (2018).

651 2. Ayad, N. M. E., Kaushik, S. & Weaver, V. M. Tissue mechanics, an important regulator of development and
652 disease. Philosophical Transactions Royal Soc B 374, 20180215 (2019).

653 3. Eichinger, J. F. et al. Mechanical homeostasis in tissue equivalents: a review. Biomech Model Mechan 20,
654 833–850 (2021).

655 4. Humphrey, J. D., Dufresne, E. R. & Schwartz, M. A. Mechanotransduction and extracellular matrix
656 homeostasis. Nat Rev Mol Cell Biology 15, 802–12 (2014).

657 5. Kozyrina, A. N., Piskova, T. & Di Russo, J. Mechanobiology of Epithelia From the Perspective of Extracellular
658 Matrix Heterogeneity. Frontiers Bioeng Biotechnology 8, 596599 (2020).

659 6. Booij, J. C., Baas, D. C., Beisekeeva, J., Gorgels, T. G. M. F. & Bergen, A. A. B. The dynamic nature of Bruch's
660 membrane. Prog Retin Eye Res 29, 1–18 (2010).

661 7. Raymond, S. M. & Jackson, I. J. The retinal pigmented epithelium is required for development and
662 maintenance of the mouse neural retina. Curr Biol 5, 1286–1295 (1995).

663 8. German, O., Buzzi, E., Rotstein, N., Rodriguez-Boulan, E. & Politi, L. Retinal pigment epithelial cells promote
664 spatial reorganization and differentiation of retina photoreceptors. J Neurosci Res 86, 3503–3514 (2008).

665 9. Bok, D. The retinal pigment epithelium: a versatile partner in vision. J Cell Sci 1993, 189–195 (1993).

666 10. Strauss, O. The Retinal Pigment Epithelium in Visual Function. Physiol Rev 85, 845–881 (2005).

667 11. Lakkaraju, A. et al. The Cell Biology of the Retinal Pigment Epithelium. Prog Retin Eye Res 78, 100846
668 (2020).

669 12. Young, R. W. & Bok, D. Partecipation of the Retinal Pigment Epithelium in the Rod Outer Segment Renewal
670 Process. J Cell Biology 42, 392–403 (1969).

671 13. Wald, G. & Brown, P. K. Synthesis and Bleaching of Rhodopsin. Nature 177, 174–176 (1956).

672 14. Volland, S., Esteve-Rudd, J., Hoo, J., Yee, C. & Williams, D. S. A Comparison of Some Organizational
673 Characteristics of the Mouse Central Retina and the Human Macula. Plos One 10, e0125631 (2015).

674 15. Bhatia, S. K. et al. Analysis of RPE morphometry in human eyes. Mol Vis 22, 898–916 (2016).

675 16. Kim, Y.-K. et al. Morphometric Analysis of Retinal Pigment Epithelial Cells From C57BL/6J Mice During
676 Aging. Invest Ophth Vis Sci 62, 32 (2021).

677 17. Ortolan, D. et al. Single-cell–resolution map of human retinal pigment epithelium helps discover
678 subpopulations with differential disease sensitivity. Proc. Natl. Acad. Sci. 119, e2117553119 (2022).

679 18. Chong, N. H. V. et al. Decreased Thickness and Integrity of the Macular Elastic Layer of Bruch's Membrane
680 Correspond to the Distribution of Lesions Associated with Age-Related Macular Degeneration. Am J
681 Pathology 166, 241–251 (2005).

682 19. Newsome, D. A., Huh, W. & Green, W. R. Bruch's membrane age-related changes vary by region. Curr Eye
683 Res 6, 1211–1221 (1987).

684 20. Hannezo, E., Prost, J. & Joanny, J.-F. Theory of epithelial sheet morphology in three dimensions. Proc
685 National Acad Sci 111, 27–32 (2014).

686 21. Alt, S., Ganguly, P. & Salbreux, G. Vertex models: from cell mechanics to tissue morphogenesis.
687 Philosophical Transactions Royal Soc B Biological Sci 372, 20150520 (2017).

688 22. Kaliman, S. et al. Mechanical Regulation of Epithelial Tissue Homeostasis. Phys Rev X 11, 031029 (2021).

689 23. Bi, D., Lopez, J. H., Schwarz, J. M. & Manning, M. L. A density-independent rigidity transition in biological
690 tissues. Nat Phys 11, 1074–1079 (2015).

691 24. Lewis, F. T. A comparison between the mosaic of polygons in a film of artificial emulsion and the pattern of
692 simple epithelium in surface view (cucumber epidermis and human amnion). Anat Rec 50, 235–265 (1931).

693 25. Lewis, F. T. The correlation between cell division and the shapes and sizes of prismatic cells in the
694 epidermis of cucumis. Anat Rec 38, 341–376 (1928).

695 26. Chiu, S. N. Aboav-Weaire's and Lewis' laws—A review. Mater Charact 34, 149–165 (1995).

696 27. Kim, S., Cai, M. & Hilgenfeldt, S. Lewis' law revisited: the role of anisotropy in size–topology correlations.
697 New J Phys 16, 015024 (2014).

698 28. Rivier, N. Statistical crystallography Structure of random cellular networks. Philosophical Mag Part B 52,
699 795–819 (2006).

700 29. Aboav, D. A. The arrangement of cells in a net. Metallography 13, 43–58 (1980).

701 30. Aboav, D. A. The arrangement of grains in a polycrystal. Metallography 3, 383–390 (1970).

702 31. Weaire, D. Some remarks on the arrangement of grains in a polycrystal. Metallography 7, 157–160 (1974).

703 32. Song, M. J. et al. Bioprinted 3D outer retina barrier uncovers RPE-dependent choroidal phenotype in
704 advanced macular degeneration. Nat Methods 20, 149–161 (2023).

705 33. Müller, C., Charniga, C., Temple, S. & Finnemann, S. C. Quantified F-Actin Morphology Is Predictive of
706 Phagocytic Capacity of Stem Cell-Derived Retinal Pigment Epithelium. Stem Cell Rep 10, 1075–1087 (2018).

707 34. Przybyla, L., Lakins, J. N., Sunyer, R., Trepat, X. & Weaver, V. M. Monitoring developmental force
708 distributions in reconstituted embryonic epithelia. Methods 94, 101–113 (2016).

709 35. Funaki, M. & Janmey, P. A. Biology and Engineering of Stem Cell Niches. Part Iii Des Smart Biomaterials
710 Mimic Control Stem Cell Niche 363–373 (2017) doi:10.1016/b978-0-12-802734-9.00023-8.

711 36. Di Russo, J. et al. Integrin α5β1 nano-presentation regulates collective keratinocyte migration independent
712 of substrate rigidity. Elife 10, e69861 (2021).

713 37. Vishwakarma, M. et al. Mechanical interactions among followers determine the emergence of leaders in
714 migrating epithelial cell collectives. Nat Commun 9, 3469 (2018).

715 38. Park, J.-A. A. et al. Unjamming and cell shape in the asthmatic airway~epithelium. Nat Mater 14, 1040–8
716 (2015).

717 39. Malinverno, C. et al. Endocytic reawakening of motility in jammed epithelia. Nat Mater 16, 587 (2017).

718 40. Palamidessi, A. et al. Unjamming overcomes kinetic and proliferation arrest in terminally differentiated
719 cells and promotes collective motility of carcinoma. Nat Mater 18, 1252–1263 (2019).

720 41. Balcioglu, H. E. et al. A subtle relationship between substrate stiffness and collective migration of cell
721 clusters. Soft Matter 16, 1825–1839 (2020).

722 42. Mongera, A. et al. A fluid-to-solid jamming transition underlies vertebrate body axis elongation. Nature
723 (2018) doi:10.1038/s41586-018-0479-2.

724 43. Pérez-González, C. et al. Mechanical compartmentalization of the intestinal organoid enables crypt folding
725 and collective cell migration. Nat Cell Biol 1–13 (2021) doi:10.1038/s41556-021-00699-6.

726 44. Di Russo, J., Magin, T. M. & Leube, R. E. A keratin code defines the textile nature of epithelial tissue
727 architecture. Curr. Opin. Cell Biol. 85, 102236 (2023).

728 45. Alberts, B. et al. Molecular Biology of the Cell. 43–108 (2017) doi:10.1201/9781315735368-2.

729 46. Aumailley, M. The laminin family. Cell Adhes Migr 7, 48–55 (2012).

730 47. Hynes, R. O. Integrins Bidirectional, Allosteric Signaling Machines. Cell 110, 673–687 (2002).

731 48. Wang, W. et al. Hemidesmosomes modulate force generation via focal adhesions. J Cell Biol 219,
732 e201904137 (2020).

733 49. Kechagia, Z. et al. The laminin–keratin link shields the nucleus from mechanical deformation and signalling.
734 Nat. Mater. 1–12 (2023) doi:10.1038/s41563-023-01657-3.

735 50. Moch, M. & Leube, R. E. Hemidesmosome-Related Keratin Filament Bundling and Nucleation. Int. J. Mol.
736 Sci. 22, 2130 (2021).

737 51. Schwarz, N., Windoffer, R., Magin, T. & Leube, R. Dissection of keratin network formation, turnover and
738 reorganization in living murine embryos. Sci Rep-uk 5, 9007 (2015).

739 52. Windoffer, R. et al. Quantitative mapping of keratin networks in 3D. Elife 11, e75894 (2022).

740 53. Nobeschi, L., Freymuller, E. & Smith, R. L. Intercellular Junctions in Rabbit Eye Ora Serrata. Anatomia
741 Histologia Embryologia 35, 287–292 (2006).

742 54. Di Russo, J. et al. Endothelial basement membrane laminin 511 is essential for shear stress response. Embo
743 J 36, 183–201 (2016).

744 55. Song, J. et al. Endothelial Basement Membrane Laminin 511 Contributes to Endothelial Junctional
745 Tightness and Thereby Inhibits Leukocyte Transmigration. Cell Reports 18, 1256–1269 (2017).

746 56. Hahn, B.-S. & Labouesse, M. Tissue integrity: Hemidesmosomes and resistance to stress. Curr Biol 11,
747 R858–R861 (2001).

748 57. Todorović, V., Kligys, K. R., Dusek, R. L., Jones, J. C. R. & Green, K. J. Encyclopedia of Biological Chemistry
749 (Second Edition). Cell Archit Funct Article Titles D 636–643 (2013) doi:10.1016/b978-0-12-378630-2.00472-
750 2.

751 58. Broussard, J. A. et al. Scaling up single-cell mechanics to multicellular tissues – the role of the intermediate
752 filament–desmosome network. J Cell Sci 133, jcs228031 (2020).

753 59. Ingber, D. E., Wang, N. & Stamenović, D. Tensegrity, cellular biophysics, and the mechanics of living
754 systems. Rep Prog Phys 77, 046603 (2014).

755 60. Rölleke, U., Kumari, P., Meyer, R. & Köster, S. The unique biomechanics of intermediate filaments – From
756 single filaments to cells and tissues. Curr. Opin. Cell Biol. 85, 102263 (2023).

757 61. Oria, R. et al. Force loading explains spatial sensing of ligands by cells. Nature 552, 219–224 (2017).

758 62. Anderson, R. E., Vail, M. M. L. & Hollyfield, J. G. Degenerative Diseases of the Retina. 1, (1995).

759 63. Kwon, W. & Freeman, S. A. Phagocytosis by the Retinal Pigment Epithelium: Recognition, Resolution,
760 Recycling. Front Immunol 11, 604205 (2020).

761 64. Jaumouillé, V., Cartagena-Rivera, A. X. & Waterman, C. M. Coupling of β2 integrins to actin by a
762 mechanosensitive molecular clutch drives complement receptor-mediated phagocytosis. Nat Cell Biol 21,
763 1357–1369 (2019).

764 65. Al-Humimat, G., Marashdeh, I., Daradkeh, D. & Kooner, K. Investigational Rho Kinase Inhibitors for the
765 Treatment of Glaucoma. J. Exp. Pharmacol. 13, 197–212 (2021).

766 66. Mandell, K. J., Kudelka, M. R. & Wirostko, B. Rho kinase inhibitors for treatment of glaucoma. Expert Rev.
767 Ophthalmol. 6, 611–622 (2011).

768 67. Claybon, A. & Bishop, A. J. R. Dissection of a Mouse Eye for a Whole Mount of the Retinal Pigment
769 Epithelium. J Vis Exp (2011) doi:10.3791/2563.

770 68. Stringer, C., Wang, T., Michaelos, M. & Pachitariu, M. Cellpose: a generalist algorithm for cellular
771 segmentation. Nat Methods 18, 100–106 (2021).

772 69. Kaliman, S., Jayachandran, C., Rehfeldt, F. & Smith, A.-S. Limits of Applicability of the Voronoi Tessellation
773 Determined by Centers of Cell Nuclei to Epithelium Morphology. Front Physiol 7, 551 (2016).

774 70. Parinot, C., Rieu, Q., Chatagnon, J., Finnemann, S. C. & Nandrot, E. F. Large-Scale Purification of Porcine or
775 Bovine Photoreceptor Outer Segments for Phagocytosis Assays on Retinal Pigment Epithelial Cells. J Vis Exp
776 (2014) doi:10.3791/52100.

777

778

SUPPLEMENTARY INFORMATION

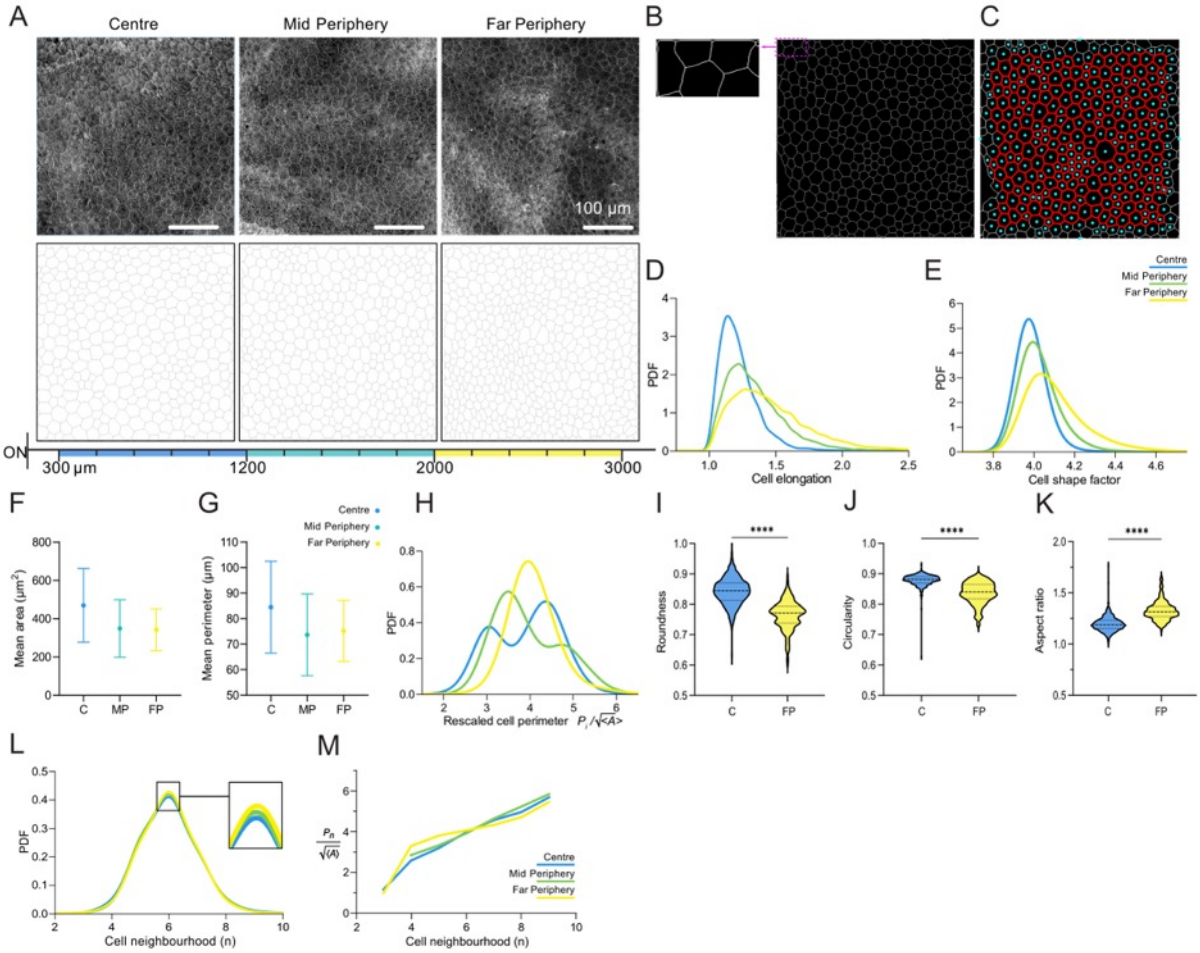

Supplementary figure 1: Murine RPE represents spatially different monolayer organisation. ***(A)*** *Representative confocal images of RPE stained for F-actin (top row) and post-processed binary images obtained by skeletisation used for the morphometric characterisation upon segmentation (bottom row). Scale bar 100 µm.* ***(B)*** *Representative segmentation artefacts generated with Cellpose at the image edge.* ***(C)*** *The resulting cells (blue) and neighbourhood (red) considered in the analyses. Probability density function (PDF) of cell elongation* ***(D)*** *and cell shape factor* ***(E)*** *for different retinal regions. The average cellular area* ***(F)*** *and perimeter* ***(G)*** *shown with mean value and standard deviation for each region, respectively.* ***(H)*** *PDF of the rescaled cell perimeters defined as* $P_i/\sqrt{< A >}$*, Pi being the individual cell perimeter. Nuclear geometric parameters such as roundness* ***(I)****, circularity* ***(J)*** *and elliptical aspect ratio* ***(K)*** *show significant difference for cells from centre versus far periphery. Topological characteristics of the RPE monolayer such as PDF of cell neighbourhood* ***(L)*** *and Desh's law* ***(M)*** *representing the relationship between cellular perimeter and shape varying for three different regions. All data were collected from at least 3 mice.*

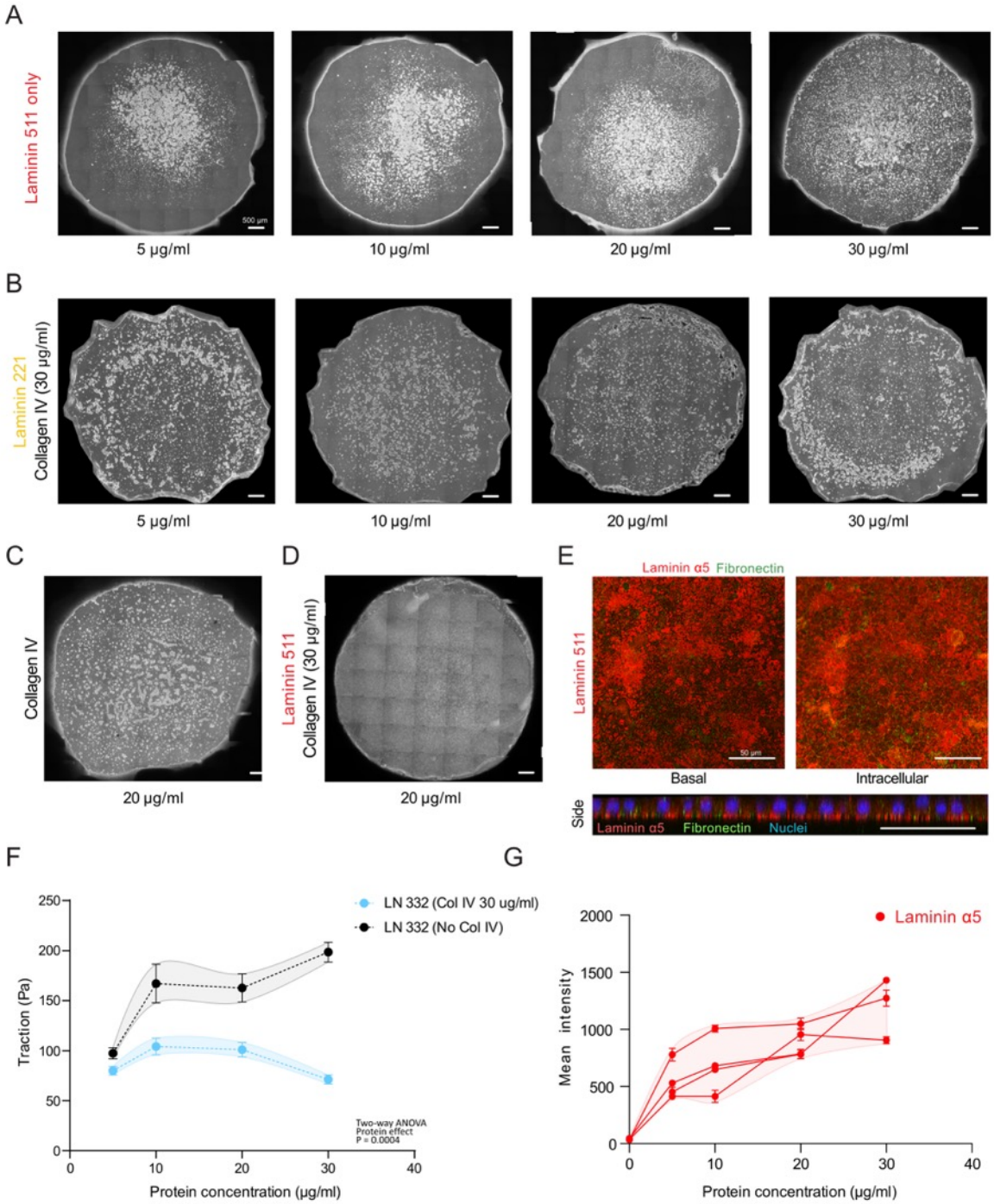

781 ***Supplementary figure 1: Protein composition of polyacrylamide gel surface coating is crucial for cell adhesion strength.*** *Representative overview images of colonies hiPSC-RPE cells seeded on 4 kPa polyacrylamide gel coated with different concentrations of laminin 511* ***(A)*** *and laminin 221 combined with collagen type IV (30 µg/ml)* ***(B)*** *and pure collagen type IV (20 µg/ml)* ***(C)*** *indicating the insufficient cellular adhesion and monolayer formation in contrast to standard experimental conditions* ***(D)****. Scale bar 500 µm.* ***(E)*** *Immunofluorescent images of the laminin 511 coated gel surface stained for ECM proteins show the absence of fibronectin protein deposition after one week in cellular culture. Top row represents the signal from laminin α5 (red) and fibronectin (green) at the basal surface and within the monolayer. Fibronectin signal appears to be intracellular as shown in the side view of the monolayer.* ***(F)*** *The presence of collagen type IV in the laminin 332 containing coating solution decreases the traction forces exerted by cells. This difference becomes less significant at lower laminin concentration.* ***(G)*** *Line graph of the mean fluorescent intensity of the hydrogel surface fixed and stained with laminin α5 antibody right after chemical crosslinking with different concentrations of laminin 511 combined with collagen type IV (30 µg/ml). This relation indicates correlation between laminin concentration and surface density. Each line represents individual dilution series, images were taken from 10 different areas of the gel. Data are shown as mean ± SEM. ***p=0.0004 for the protein effect using mixed-effects model (REML) with the Geisser-Greenhouse correction and Tuckey's multiple comparisons test (F, G).*

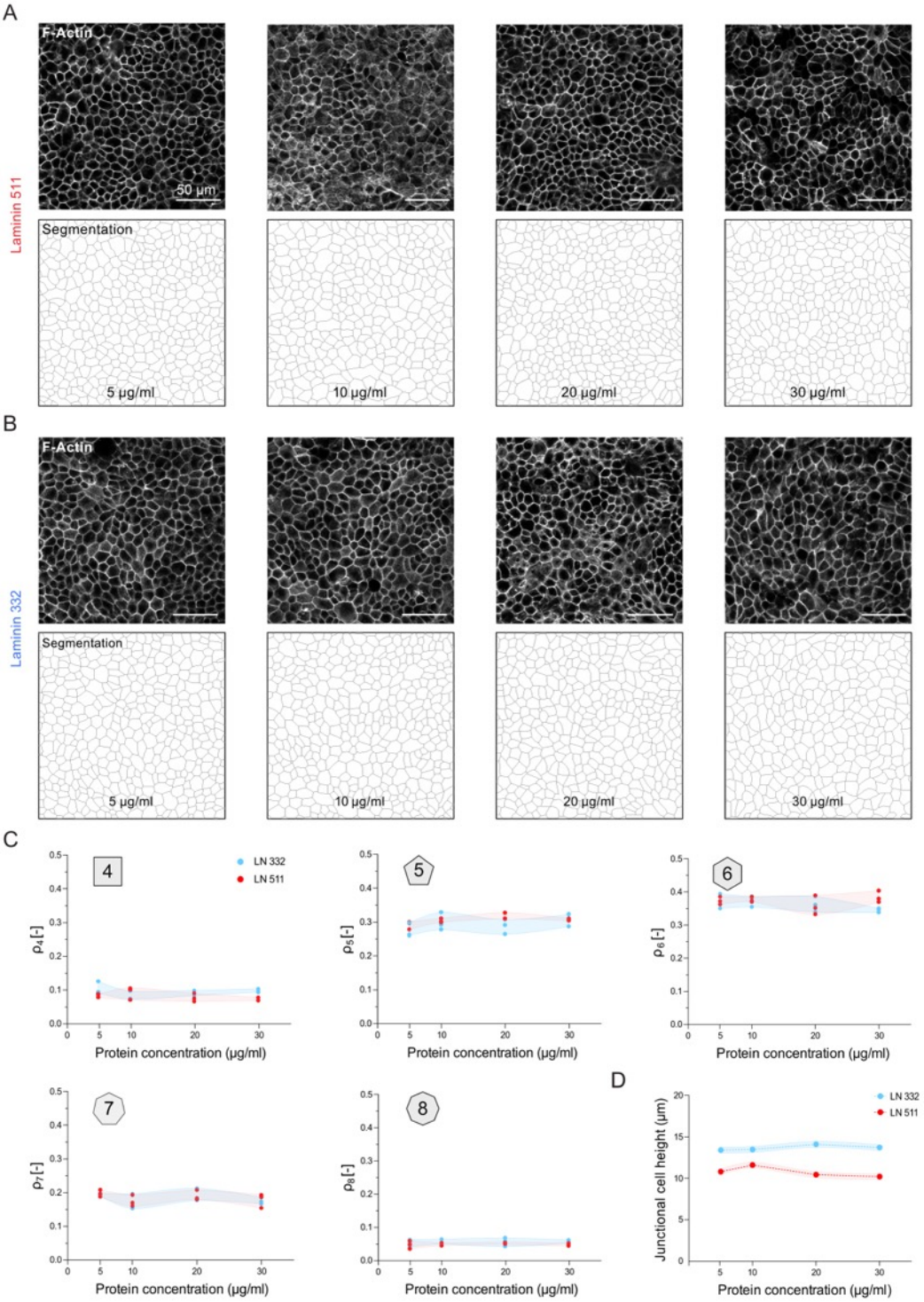

Supplementary figure 2: Structure and topological stability of RPE in vitro. *Representative confocal images of one-week cultured hiPSC-RPE monolayers on 4 kPa PAA gels coated with different concentrations of laminin 511* ***(A)*** *or laminin 332* ***(B)*** *both in presence of collagen type IV (30 µg/ml). The top row represents the actin cytoskeleton network in the stained samples and the bottom row shows segmented images used for morphometric analysis.* ***(C)*** *Probabilities of the cellular neighbourhood (ρ_n) from 4 (ρ_4) "squares" to 8 (ρ_8) "octagon" indicating the stable neighbourhood environment regardless of the protein surface concentration. Data are from 3 independent experiments with 3 independent fields of view in each experiment.* ***(D)*** *Average cell height measured at the adherence junction levels. Measurements are means from at least three independent experiments ± SEM.*

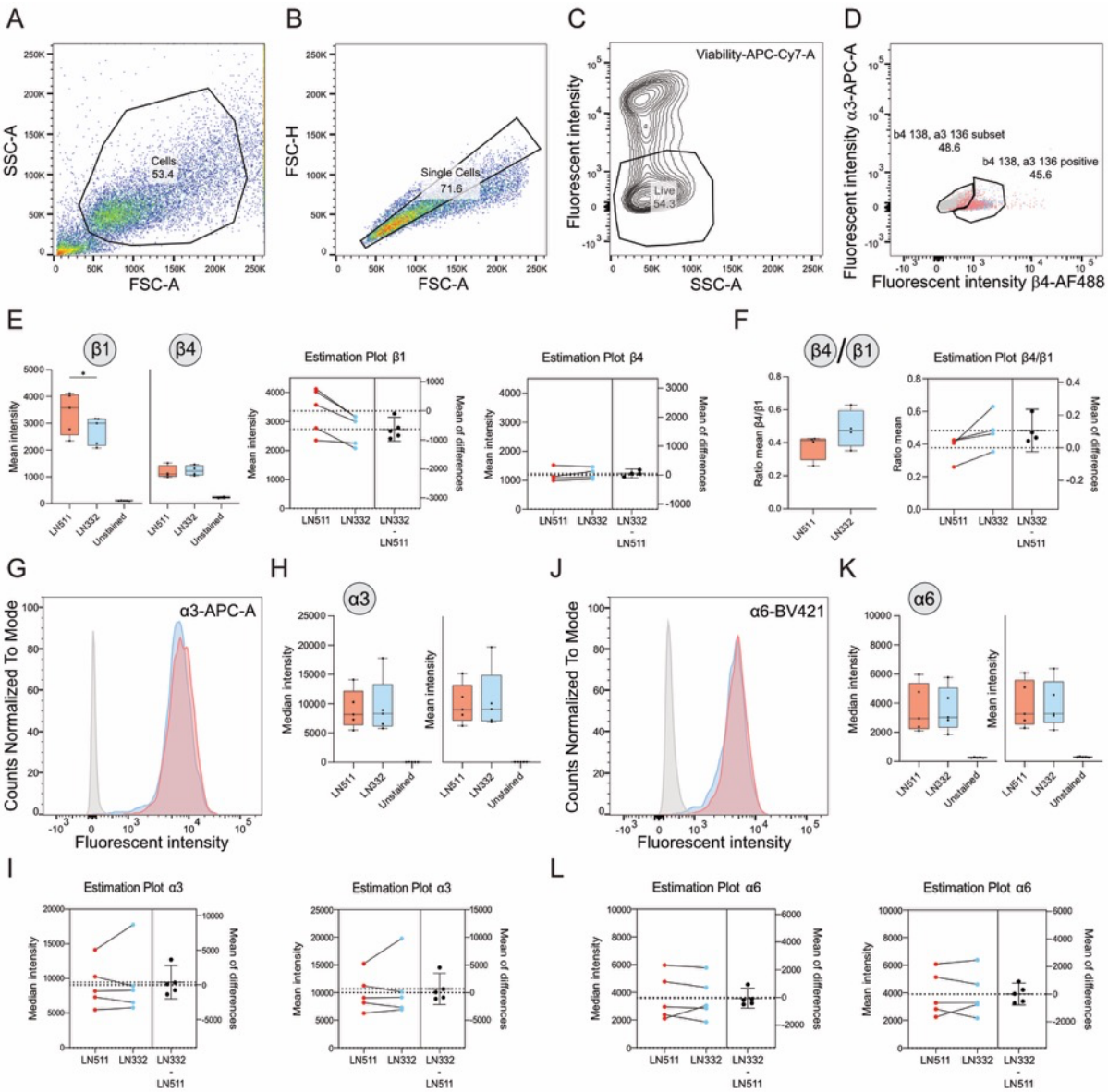

783
784

Supplementary figure 4: Flow cytometry analysis of hiPSC-RPE cultured on polyacrylamide gels coated with 5 µg/ml of laminin 511 or laminin 332. *Representative dot plots showing the gating strategy to identify cells* ***(A)****, single cells* ***(B),*** *contour plot to extract a population of single living cells* ***(C)*** *and gating strategy for β4-positive cells* ***(D)****.* ***(E)*** *Box and whisker plots of the mean intensity of integrin β1 and integrin β4 staining (left) and corresponding estimation plots (right) acquired from flow cytometry data.* ***(F)*** *Box and whisker (left) and estimation (right) plots showing the ratio between mean intensity of integrin β4 and integrin β1 staining. Representative histograms of flow cytometry analysis, box and whisker plots of median and mean fluorescent intensity and corresponding estimation plots of staining for APC-A-conjugated integrin α3* ***(G, H and I)*** *and BV421-conjugated integrin α6* ***(J, K and L)****. The grey-coloured histogram represents the signal from unstained cells. Statistical analysis was done using a paired t-test to compare results between laminin 511 and laminin 332 coatings.*

785 *Table 1: List of antibodies used in this work.*

Name	Origin	Source	Concentration (µg/ml) / Dilution
Primary antibodies			
Anti mouse laminin 111 (pan-Laminin)	rabbit	Gift from Lydia Sorokin	Rabbit serum, 1:2000
Anti mouse laminin α1 (clone 200)	rat	Gift from Lydia Sorokin	Hybridoma supernatant
Anti mouse laminin α2 (clone 4H8-2)	rat	Gift from Lydia Sorokin	Hybridoma supernatant
Anti human laminin 332	rabbit	Gift from Monique Aumailley	Rabbit serum, 1:2000
Anti mouse laminin α4	rabbit	Gift from Lydia Sorokin	Rabbit serum, 1:1000
Anti mouse laminin α5	rabbit	Gift from Lydia Sorokin	Rabbit serum, 1:1000
Anti mouse collagen type IV	mouse	Merck Millipore, AB756P	12.5
Anti mouse collagen type I	rabbit	Novusbio, NB600-408	5
Anti mouse elastin	rabbit	Abcam, ab21610	5
Phalloidin iFluor 647		Abcam, ab176753	1x
Phalloidin iFluor 488		Abcam, ab176759	1x
Ant human ZO-1	rabbit	Thermo Fisher, 61-7300	5
Anti human ezrin (clone 3C12)	mouse	Abcam, ab4069	20
Anti human fibronectin	rabbit	Sigma, F3648	2.5
Antibodies used for flow cytometry			
Integrin β1-PE (clone 12G10)	mouse	Santa Cruz, sc-59827 PE	1 mg per million cells
Integrin β4-Alexa Flour 488 (clone A9)	mouse	Santa Cruz, sc-13543 AF488	1 mg per million cells
Integrin α3-Alexa Flour 647 (clone P1B5)	mouse	Santa Cruz, sc-13545 AF647	1 mg per million cells
Integrin α6-Brilliant Violet 421 (clone GOH3)	rat	BioLegend, 313623	5 ml per million cells
Secondary antibodies			
Anti-mouse-IgG AF488	goat	Invitrogen, A11001	4
Anti-mouse-IgG AF594	goat	Invitrogen, A11005	4
Anti-mouse-IgG AF647	goat	Jackson/Dianova, 111-605-144	10
Anti-rabbit-IgG AF594	goat	Invitrogen, A11012	4
Anti-rabbit-IgG AF647	goat	Molecular Probes, A21235	10
Anti-rat-IgG AF555	goat	Invitrogen, A21434	4
Anti-rat-IgG AF647	goat	Thermo Fisher, A21247	10

786
787

Table 2: Number of cells in vitro analysed for morphometric and topological parameters

	Laminin 322			Laminin 511		
	Exp 1	Exp 2	Exp 3	Exp 1	Exp 2	Exp 3
5 µg/mL	440 (454)	638 (654)	715 (736)	606 (625)	686 (710)	727 (753)
10 µg/mL	479 (495)	697 (719)	654 (679)	547 (561)	575 (594)	396 (415)
20 µg/mL	627 (641)	683 (698)	608 (634)	559 (572)	831 (856)	480 (499)
30 µg/mL	529 (539)	325 (334)	637 (660)	513 (525)	710 (737)	759 (782)

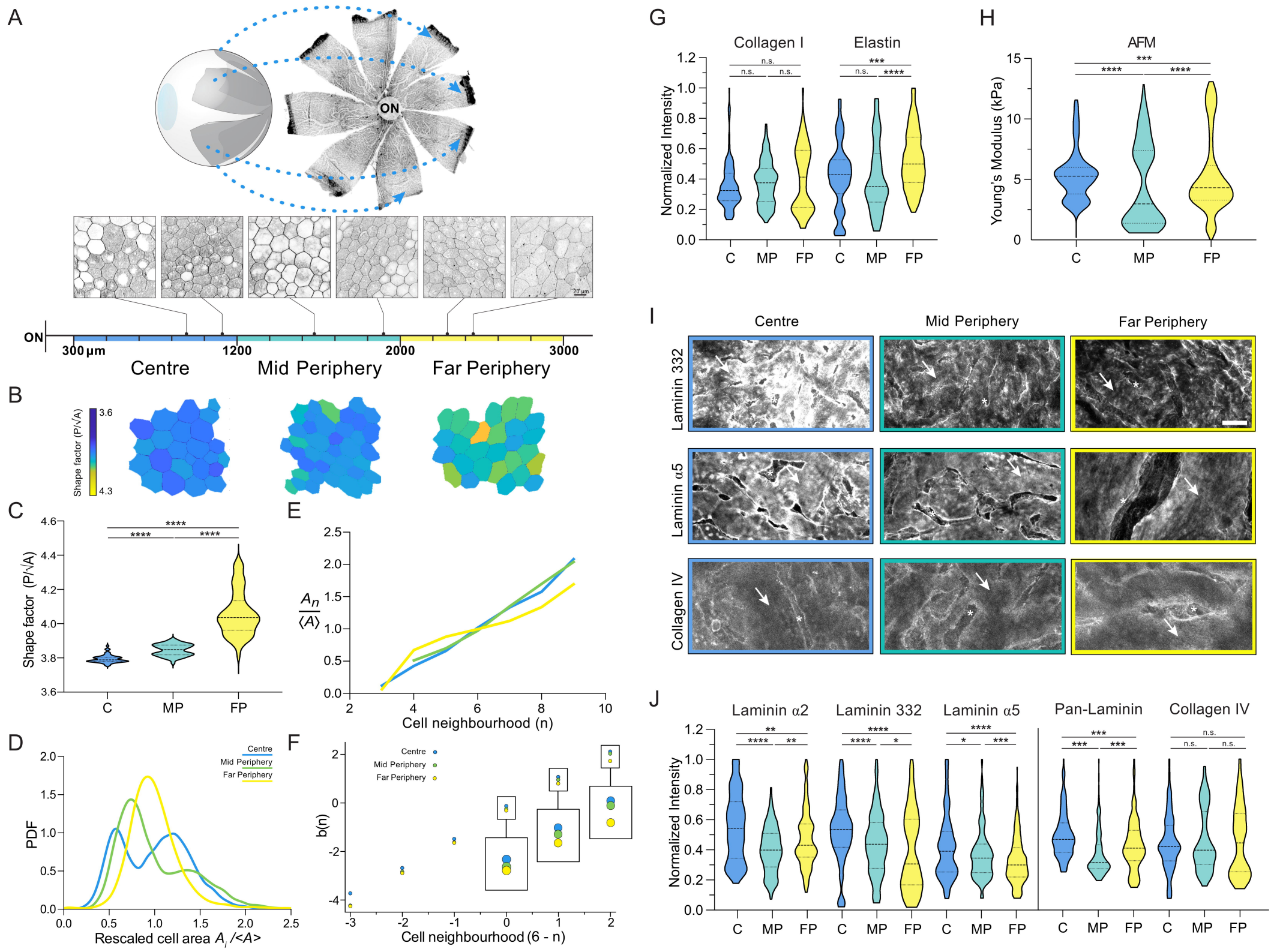
A
ON
20 µm
ON
300 µm
1200
2000
3000
Centre
Mid Periphery
Far Periphery
B
Shape factor (P/√A)
3.6
4.3
C
Shape factor (P/√A)
C
MP
FP
D
PDF
Rescaled cell area A_i /<A>
Centre
Mid Periphery
Far Periphery
E
$\frac{A_n}{\langle A \rangle}$
Cell neighbourhood (n)
F
b(n)
Cell neighbourhood (6 - n)
Centre
Mid Periphery
Far Periphery
G
Collagen I
Elastin
Normalized Intensity
n.s.
***
****
H
AFM
Young's Modulus (kPa)
I
Centre
Mid Periphery
Far Periphery
Laminin 332
Laminin α5
Collagen IV
J
Laminin α2
Laminin 332
Laminin α5
Pan-Laminin
Collagen IV
Normalized Intensity

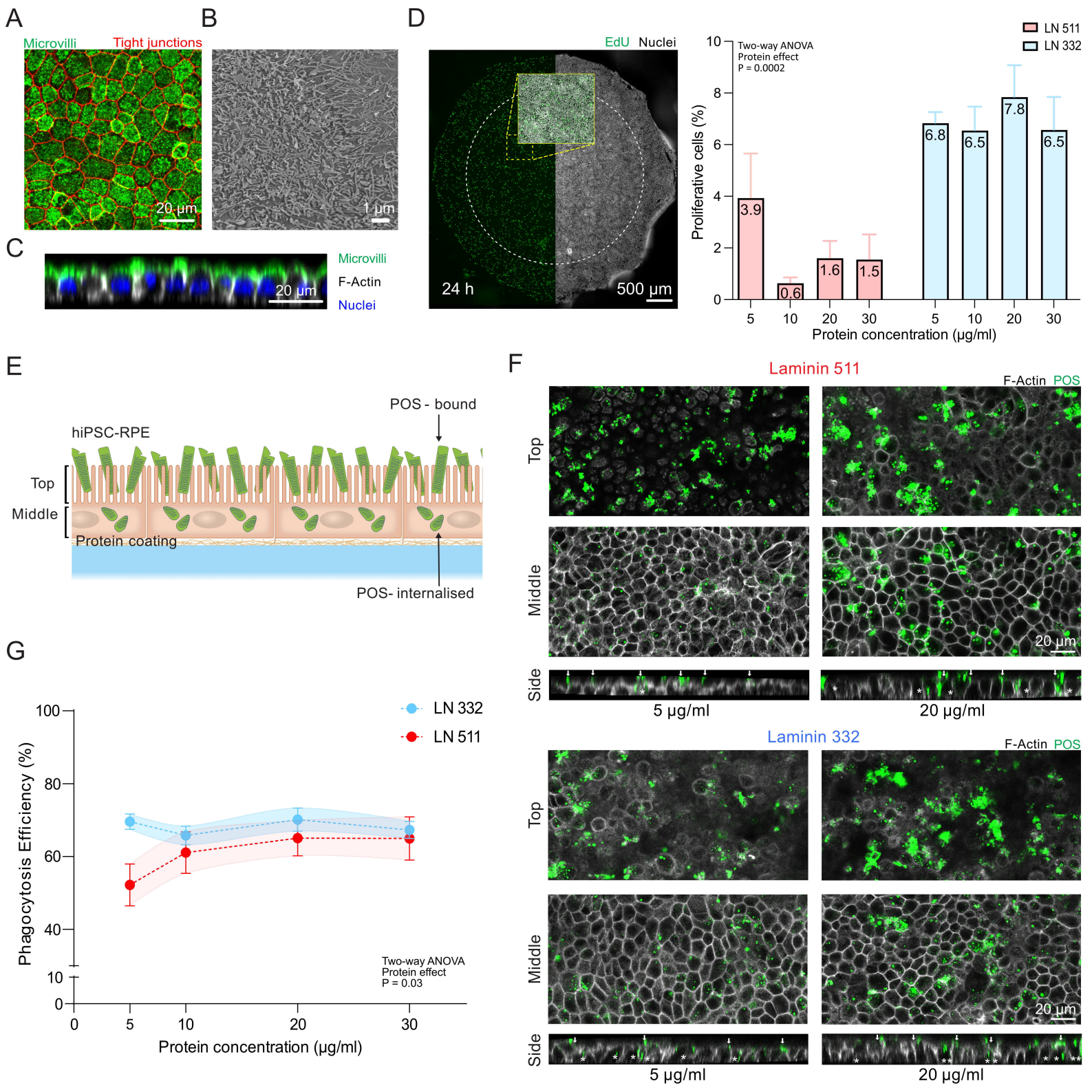
A
Microvilli
Tight junctions
20 µm
B
1 µm
C
Microvilli
F-Actin
Nuclei
20 µm
D
EdU
Nuclei
24 h
500 µm
LN 511
LN 332
Two-way ANOVA
Protein effect
P = 0.0002
Proliferative cells (%)
3.9
0.6
1.6
1.5
6.8
6.5
7.8
6.5
Protein concentration (µg/ml)
E
POS - bound
hiPSC-RPE
Top
Middle
Protein coating
POS- internalised
F
Laminin 511
F-Actin
POS
Top
Middle
Side
20 µm
5 µg/ml
20 µg/ml
Laminin 332
F-Actin
POS
Top
Middle
Side
20 µm
5 µg/ml
20 µg/ml
G
LN 332
LN 511
Phagocytosis Efficiency (%)
Two-way ANOVA
Protein effect
P = 0.03
Protein concentration (µg/ml)

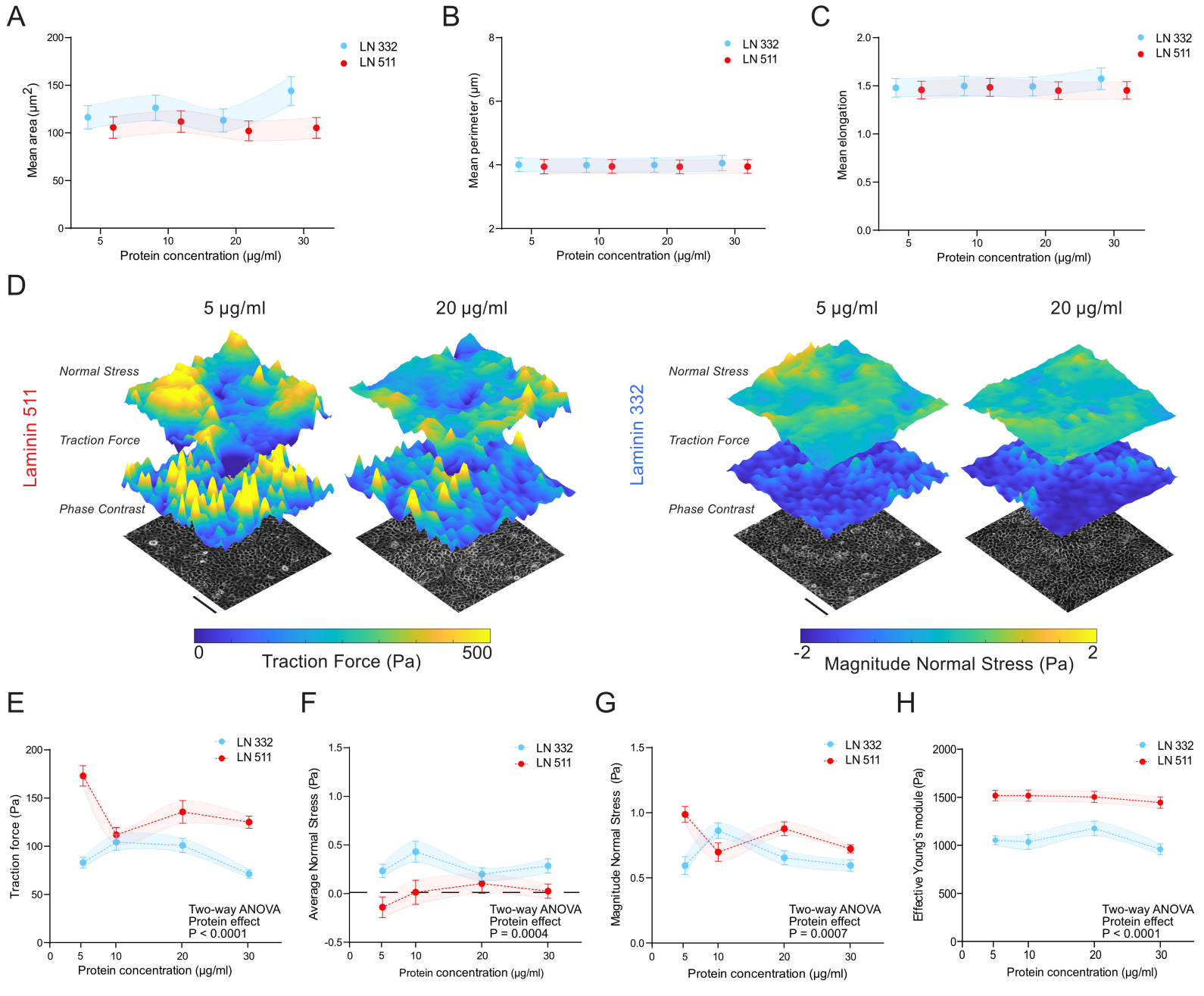
A
Mean area (μm²)
Protein concentration (μg/ml)
LN 332
LN 511
B
Mean perimeter (μm)
Protein concentration (μg/ml)
LN 332
LN 511
C
Mean elongation
Protein concentration (μg/ml)
LN 332
LN 511
D
5 μg/ml
20 μg/ml
Laminin 511
Normal Stress
Traction Force
Phase Contrast
0
500
Traction Force (Pa)
5 μg/ml
20 μg/ml
Laminin 332
Normal Stress
Traction Force
Phase Contrast
-2
2
Magnitude Normal Stress (Pa)
E
Traction force (Pa)
Protein concentration (μg/ml)
LN 332
LN 511
Two-way ANOVA
Protein effect
P < 0.0001
F
Average Normal Stress (Pa)
Protein concentration (μg/ml)
LN 332
LN 511
Two-way ANOVA
Protein effect
P = 0.0004
G
Magnitude Normal Stress (Pa)
Protein concentration (μg/ml)
LN 332
LN 511
Two-way ANOVA
Protein effect
P = 0.0007
H
Effective Young's module (Pa)
Protein concentration (μg/ml)
LN 332
LN 511
Two-way ANOVA
Protein effect
P < 0.0001

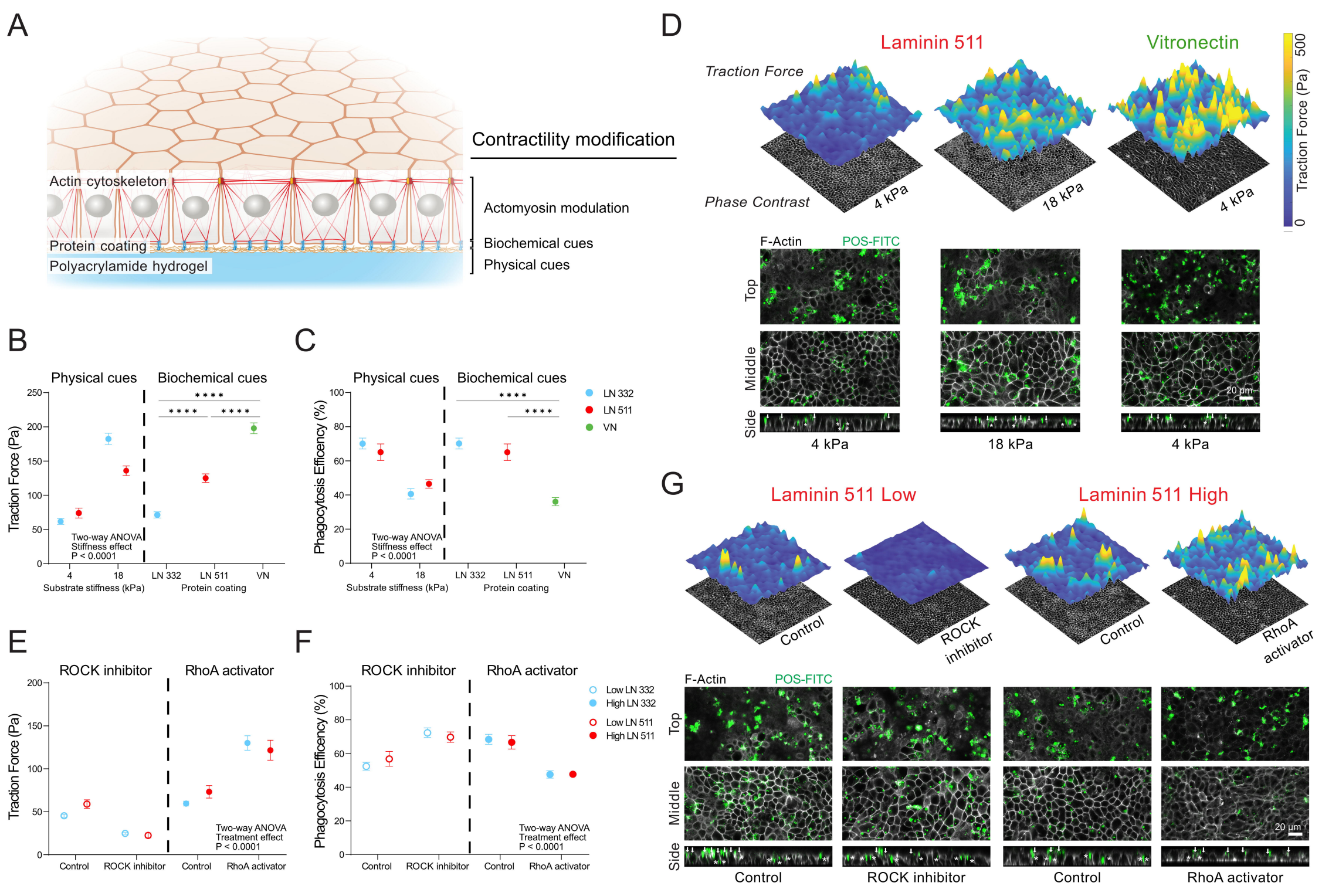
A
Contractility modification
Actin cytoskeleton
Protein coating
Polyacrylamide hydrogel
Actomyosin modulation
Biochemical cues
Physical cues
B
Physical cues
Biochemical cues
Traction Force (Pa)
Two-way ANOVA
Stiffness effect
P < 0.0001
Substrate stiffness (kPa)
Protein coating
LN 332
LN 511
VN
C
Phagocytosis Efficency (%)
Two-way ANOVA
Stiffness effect
P < 0.0001
D
Laminin 511
Vitronectin
Traction Force
Phase Contrast
4 kPa
18 kPa
Traction Force (Pa)
F-Actin
POS-FITC
Top
Middle
Side
20 µm
E
ROCK inhibitor
RhoA activator
Two-way ANOVA
Treatment effect
P < 0.0001
Control
F
Low LN 332
High LN 332
Low LN 511
High LN 511
G
Laminin 511 Low
Laminin 511 High
Control
ROCK inhibitor
RhoA activator

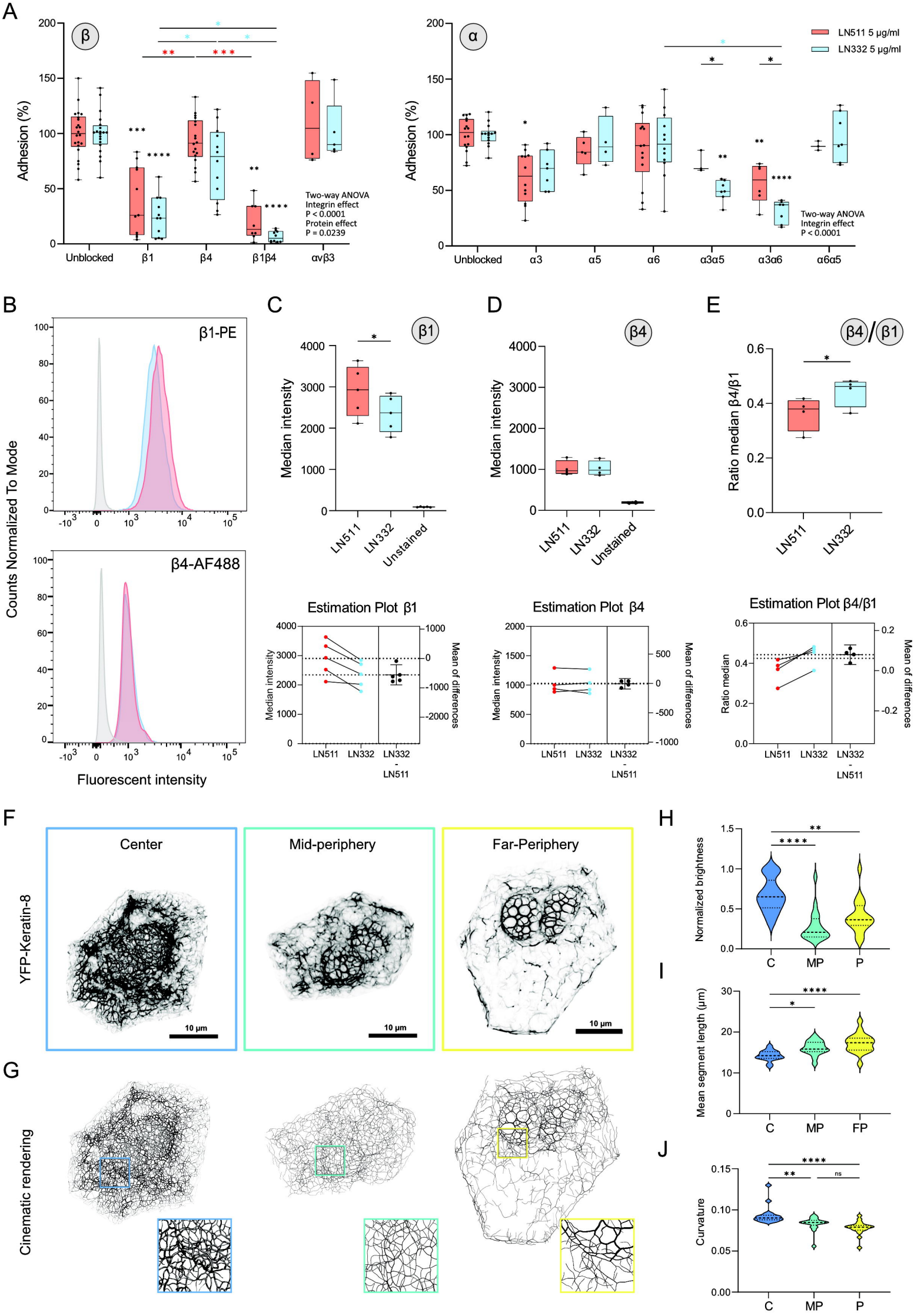
A
β
Adhesion (%)
Unblocked
β1
β4
β1β4
αvβ3
Two-way ANOVA
Integrin effect
P < 0.0001
Protein effect
P = 0.0239
α
LN511 5 µg/ml
LN332 5 µg/ml
Unblocked
α3
α5
α6
α3α5
α3α6
α6α5
Two-way ANOVA
Integrin effect
P < 0.0001
B
β1-PE
β4-AF488
Counts Normalized To Mode
Fluorescent intensity
C
β1
Median intensity
LN511
LN332
Unstained
Estimation Plot β1
Mean of differences
D
β4
Estimation Plot β4
E
β4/β1
Ratio median β4/β1
Estimation Plot β4/β1
Ratio median
F
Center
Mid-periphery
Far-Periphery
YFP-Keratin-8
10 µm
G
Cinematic rendering
H
Normalized brightness
C
MP
P
I
Mean segment length (µm)
FP
J
Curvature
ns

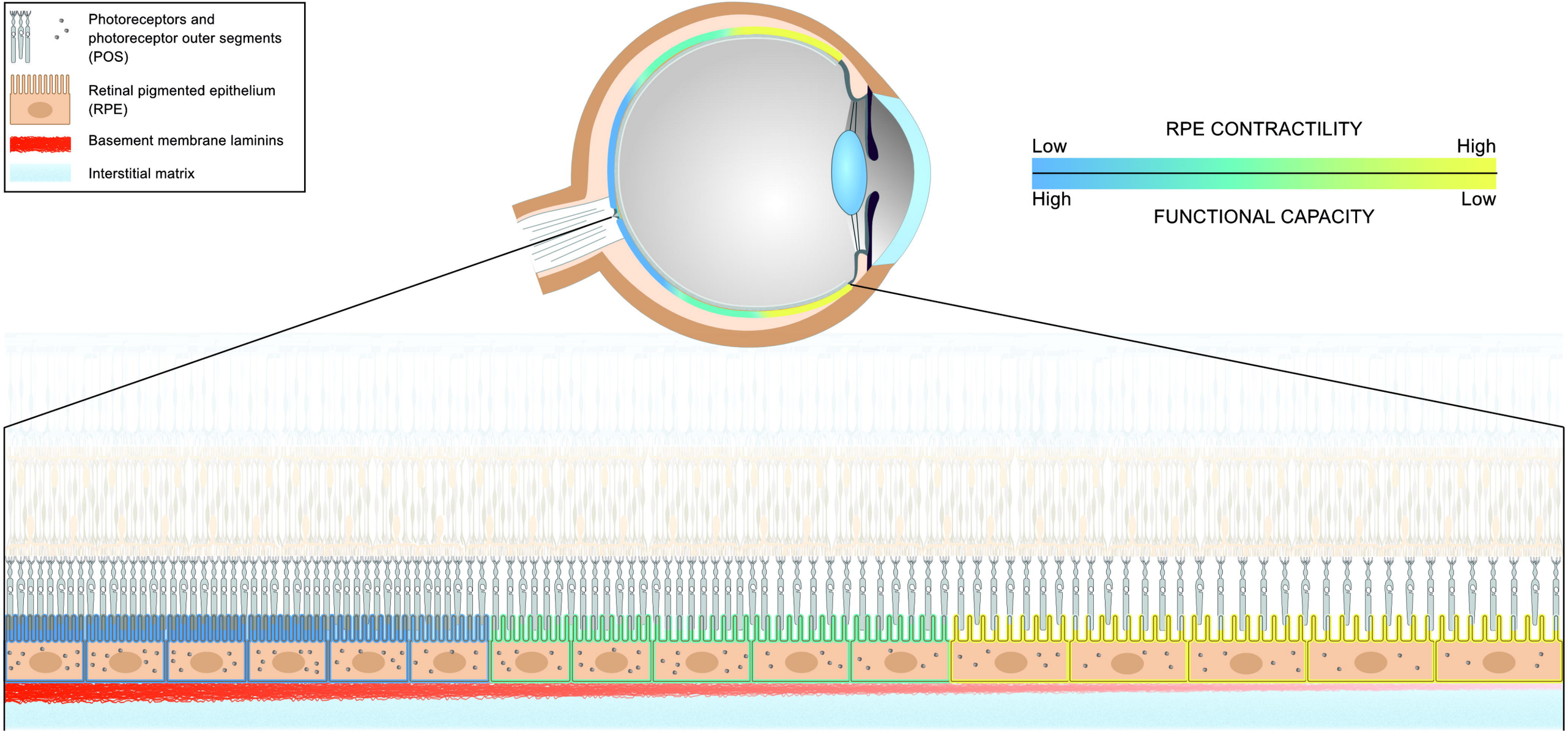
Photoreceptors and photoreceptor outer segments (POS)
Retinal pigmented epithelium (RPE)
Basement membrane laminins
Interstitial matrix
RPE CONTRACTILITY
Low
High
High
Low
FUNCTIONAL CAPACITY